

Spectroscopically resolved partial phase curve of the rapid heating and cooling of the highly-eccentric Hot Jupiter HAT-P-2b with WFC3

BOB JACOBS ^{1,2}, JEAN-MICHEL DÉSSERT ¹, NIKOLE LEWIS ³, RYAN C. CHALLENGER ³, L. C. MAYORGA ⁴, ZOË L. DE BEURS ^{5,6},
VIVIEN PARMENTIER,⁷ KEVIN B. STEVENSON ⁴, JULIEN DE WIT ⁵, SAUGATA BARAT ¹, JONATHAN FORTNEY,⁸ TIFFANY KATARIA ⁹ AND
MICHAEL LINE¹⁰

¹*Anton Pannekoek Institute for Astronomy, University of Amsterdam, Science Park 904, 1098 XH, Amsterdam, the Netherlands*

²*Department of Astrophysics/IMAPP, Radboud University, PO Box 9010, 6500 GL Nijmegen, The Netherlands*

³*Department of Astronomy and Carl Sagan Institute, Cornell University, 122 Sciences Drive, Ithaca, NY 14853, USA*

⁴*Johns Hopkins University Applied Physics Laboratory, 11100 Johns Hopkins Rd, Laurel, MD, 20723, USA*

⁵*Department of Earth, Atmospheric and Planetary Sciences, Massachusetts Institute of Technology, Cambridge, MA 02139, USA*

⁶*NSF Graduate Research Fellow, MIT Presidential Fellow, MIT Collamore-Rogers Fellow*

⁷*Laboratoire Lagrange, Observatoire de la Côte d'Azur, Université Côte d'Azur, Nice, France*

⁸*Department of Astronomy and Astrophysics, University of California, Santa Cruz, 95064, CA, USA*

⁹*NASA Jet Propulsion Laboratory, California Institute of Technology, Pasadena, CA 91109, USA*

¹⁰*School of Earth and Space Exploration, Arizona State University, Tempe, AZ 85287, USA*

Submitted to AJ

ABSTRACT

The extreme environments of transiting close-in exoplanets in highly-eccentric orbits are ideal for testing exo-climate physics. Spectroscopically resolved phase curves not only allow for the characterization of their thermal response to irradiation changes but also unveil phase-dependent atmospheric chemistry and dynamics. We observed a partial phase curve of the highly-eccentric close-in giant planet HAT-P-2b ($e = 0.51$, $M = 9M_{\text{Jup}}$) with the Wide Field Camera 3 aboard the *Hubble Space Telescope*. Using these data, we updated the planet's orbital parameters and radius, and retrieved high-frequency pulsations consistent with the planet-induced pulsations reported in Spitzer data. We found that the peak in planetary flux occurred at 6.7 ± 0.6 hr after periastron, with a heating and cooling timescales of $9.0^{+3.5}_{-2.1}$ hr, and $3.6^{+0.7}_{-0.6}$ hr, respectively. We compare the light-curve to various 1-dimensional and 3-dimensional forward models, varying the planet's chemical composition. The strong contrast in flux increase and decrease timescales before and after periapse indicates an opacity term that emerges during the planet's heating phase, potentially due to more H^- than expected from chemical equilibrium models. The phase-resolved spectra are largely featureless, that we interpret as indicative an inhomogeneous dayside. However, we identified an anomalously high flux in the spectroscopic bin coinciding with the hydrogen Paschen β line and that is likely connected to the planet's orbit. We interpret this as due to shock heating of the upper atmosphere given the short timescale involved, or evidence for other star-planet interactions.

Keywords: planets and satellites: atmospheres — planets and satellites: gaseous planets

1. INTRODUCTION

The extreme nature of close-in gas giants provides a unique window into the structure and dynamics of exo-atmospheres. Due to their short periods, relative brightness, and large atmospheric scale heights close-in giants provide excellent op-

portunities to improve our understanding of exo-atmospheres through the comparison of their observations to models. Close-in exoplanets receive intense irradiation from their host stars. Their atmosphere's ability to absorb, circulate and re-emit control the evolution of the planet and their atmosphere's thermal structure.

Atmospheric composition, chemistry and dynamics are intrinsically connected. Together, they determine how a planet responds to the host star's irradiation (Showman et al. 2009;

Lewis et al. 2014). These atmospheric properties set the radiative, advective and chemical timescales; three interconnected timescales that are key to understanding the structure of exo-atmospheres. They control how an extreme variation in energy gets absorbed/emitted by the atmosphere, how the energy is redistributed over the planet and how the atmospheric composition changes (e.g. Parmentier & Crossfield 2018). These timescales are fundamental variables in dynamical atmospheric models (e.g. Iro & Deming 2010; Visscher 2012; Tsai et al. 2023). As such they are key to understanding the population of gaseous exoplanets, but they are *a priori* unknown.

Recent studies by e.g. Ehrenreich et al. (2020); Mikal-Evans et al. (2022) are starting to unveil the intrinsic 3D nature of exoplanets by finding chemical gradients across the atmosphere. Advancements in high resolution spectroscopy techniques (e.g. Pino et al. 2022) and the unprecedented precision and wavelength coverage of JWST necessitate the development and testing of 3D atmospheric models (e.g. Caldas et al. 2019; Beltz et al. 2021; Wardenier et al. 2021; Challener & Rauscher 2022).

Transiting close-in exoplanets in highly-eccentric orbits provide the ideal laboratory to test exo-atmospheric physics because their environments change rapidly through the extreme variations in insolation (e.g. de Wit et al. 2016). By spectrally resolving their phase curves one can not only characterize their response to the change in irradiation, but one can also reveal their phase-dependent chemistry and dynamics (Lewis et al. 2014; Mayorga et al. 2021; Tsai et al. 2023)

A distinct atmospheric property that arises for Hot Jupiters hotter than ~ 1700 K is the presence of a thermal inversion (Hubeny et al. 2003; Baxter et al. 2020). An atmospheric layer heats up with respect to the surrounding layers when its optical opacities exceed its infrared opacities. This creates a region where the temperature increases with decreasing pressure. Likely agents for this type of atmospheric heating in Hot Jupiters are TiO, VO, and H⁻ (Hubeny et al. 2003; Fortney et al. 2008; Lothringer et al. 2018). When the chemical timescale of the production of these molecules is short enough, eccentric planets that cross the ~ 1700 K local equilibrium temperature boundary may have a transient thermal inversion in their atmosphere (Iro & Deming 2010; Lewis et al. 2014).

HAT-P-2b is a $9.04 \pm 0.1 M_{\text{Jup}}$ planet in a highly-eccentric ($e = 0.51023$) orbit (Bakos et al. 2007; Southworth 2010; de Wit et al. 2017; de Beurs et al. 2023). Its short period (5.63 days, $a/R_s \approx 9$) causes the planet to heat up from a typical Hot Jupiter (~ 1300 K) to an Ultra-hot Jupiter (~ 2400 K) and cool down again in two Earth days (Lewis et al. 2013). Its argument of periastron ($\omega_\star \approx 190$; de Wit et al. 2017; de Beurs et al. 2023) allows us to observe primary transit just

before the heating phase and the planet’s secondary eclipse as it is cooling down quickly (see Figure 1).

Lewis et al. (2013) and de Wit et al. (2017) observed HAT-P-2b’s phase curve with the Spitzer Space telescope. At the Spitzer wavelengths (3.6, 4.5 and $8.0 \mu\text{m}$) they find that the planet’s flux peaks 4–6 hours after periastron. This shows that the planet’s atmosphere needs time to respond to the increase in incoming radiation. Lewis et al. (2013) therefore constrain the radiative timescale at mid-IR photospheric levels near periastron to be between 2 and 8 hours.

Additionally, de Wit et al. (2017) found evidence for planet-induced stellar pulsations (Bryan et al. 2024). They found two modes with respective amplitudes of 35 ± 7 ppm and 28 ± 6 ppm and frequencies of ~ 79 and ~ 91 times the orbital frequency. Furthermore, de Wit et al. (2017) found hints of apsidal precession and an evolving eccentricity in the radial velocity data. de Beurs et al. (2023) extended the baseline of radial velocity observations from 9 to 14 years and found that hints of this orbital evolution appear to persist, but additional follow-up observations are needed for confirmation. de Beurs et al. (2023) also confirmed the presence of a long-term companion of $10.7^{+5.2}_{-2.2} M_{\text{Jup}}$ in an orbit of 23.3 years.

HAT-P-2b’s phase curve is too long to feasibly observe in full. Partial phase curves of eccentric exoplanets have been observed before (Lewis et al. 2013; de Wit et al. 2016), but never spectroscopically. Kreidberg et al. (2018) spectroscopically observed two partial phase curves of the non-eccentric WASP-103b. Full phase curves include a second secondary eclipse, which sets a baseline to which stellar and telescopic variability can be compared. Partial phase curves lack an accurate baseline. Planetary day-long variations in light-curve fits therefore become degenerate with instrumental effects and/or stellar variability (Lewis et al. 2013; de Wit et al. 2017). To this end, Arcangeli et al. (2021) devised a new method to spectroscopically analyze partial phase curves that does not require *a priori* knowledge of the instrumental systematics and therefore do not require a continuous observation of the planet.

The structure of this paper is as follows: in Section 2 we first discuss the data used for this paper. We discuss how we convert the data into astrophysical signals using both light-curve fits as well as a common-mode method that retrieves phase-resolved spectra. In Section 3 we shortly describe the atmospheric models to which we compare the data. Sections 4 and 5 present the results obtained from the light-curve fits and the phase-resolved spectra respectively. We close off with a discussion on the astrophysical interpretation of our results in Section 6.

2. DATA ANALYSIS

2.1. Observations and data reduction

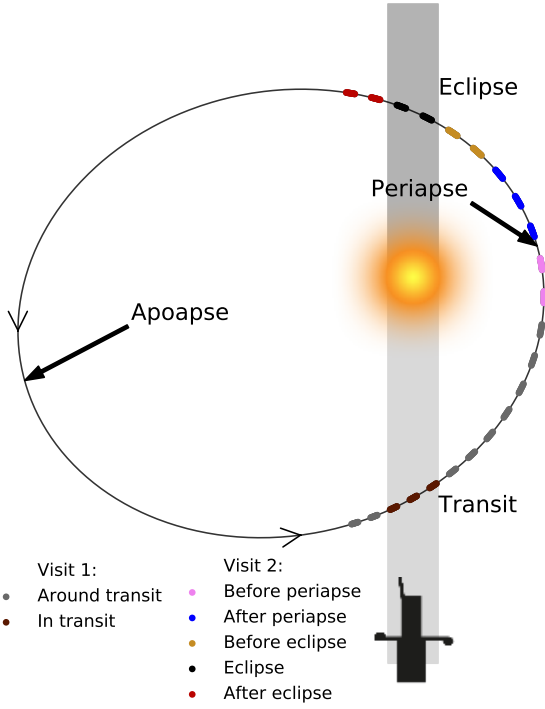


Figure 1. Visualization of HAT-P-2b’s orbit, the locations of transit, eclipse and the phases that we observed. The planet, star and orbit are to scale. We color code the HST orbits to correspond to the colors in the subsequent figures. The two visits were taken consecutively.

Our team observed HAT-P-2b for one primary transit, one secondary eclipse, and the partial phase curve in between for Program GO 16194 (PI: J.M. Désert, DOI: [10.17909/xnvc-as22](https://doi.org/10.17909/xnvc-as22)) with WFC3 in December 2020. We visualize the timing of the observations and HAT-P-2b’s orbit in Figure 1. Table 1 lists the planetary orbital phases, orbital distances, and the time after mid-transit at which the observations were made, sorted into 7 groups. The equilibrium temperatures at apoapse is 1220 K at the furthest observed orbital distance $T_{\text{eq}} = 1540$ K, and at periapse $T_{\text{eq}} = 2150$ K. The data were obtained with the G141 grism, covering 1.1 to 1.7 μm , using the bi-directional spatial scanning technique. We used the 512×512 subarray and the SPARS25, NSAMP = 8 readout mode.

The first exposure of the penultimate orbit was affected by a satellite crossing event. Like the second satellite crossing in Fu et al. (2021) and the single satellite crossing in Jacobs et al. (2022), we found no signs of its persistence impacting the remainder of the orbit. We therefore simply discarded the exposure with the satellite crossing.

We used the data reduction pipeline developed by Arcanelli et al. (2018) and updated by Jacobs et al. (2022, 2023) to convert the raw data into spectra. We picked the sixth in-eclipse exposure as our reference exposure to which we

Visit	HST orbit number	Phase	r/R_s	Time after mid-transit (hrs)	Name	
1	1	-0.035	8.7	-4.7	Around transit	
	2	-0.023	8.3	-3.1	In transit	
	3	-0.012	7.9	1.5		
	4	0.001	7.6	0.1		
	5	0.012	7.2	1.7	Around transit	
	6	0.024	6.7	3.3		
	7	0.036	6.3	4.9		
	8	0.048	5.9	6.4		
	9	0.059	5.6	8.0		
	10	0.071	5.2	9.6		
	2	11	0.083	4.9	11.2	Before periapse
		12	0.095	4.7	12.8	
13		0.106	4.5	14.4	After periapse	
14		0.118	4.5	16.0		
15		0.130	4.5	17.6		
16		0.142	4.7	19.1	Before eclipse	
17		0.153	4.9	20.7		
18		0.165	5.2	22.3	Eclipse	
19		0.177	5.6	23.9		
20		0.188	6.0	25.5		
21		0.200	6.3	27.0	After eclipse	
22		0.212	6.8	28.6		
23		0.224	7.2	30.2		

Table 1. Average planetary orbital phase, orbital distance in stellar radii, and time after mid-transit at which each HST orbit was observed. We give each group of orbits a color and a name that we will use throughout this work.

compare each exposure’s wavelength solution. Figure 2a shows the resultant raw light-curve averaged across all spectral channels in electrons per second. We call this the white light-curve.

The observations were split into two visits that were taken consecutively and without a gap, allowing for a gyro bias update in between the visits. This resulted in different telescope systematics in the flux measurements between the two visits. As the second visit has both the best pointing accuracy as well as the most interesting information, we split it further into five almost equally-sized groups of data visualized in Figure 1.

The South-Atlantic Anomaly (SAA) is a region above South America and the southern Atlantic Ocean where the cosmic ray flux levels are elevated compared to anywhere else on Earth due to a local dip in the Earth’s magnetic field. These cosmic rays strongly contaminate data, strongly impairing their reliability. Therefore, generally, no observations are taken while crossing the SAA. HST crossed the SAA dur-

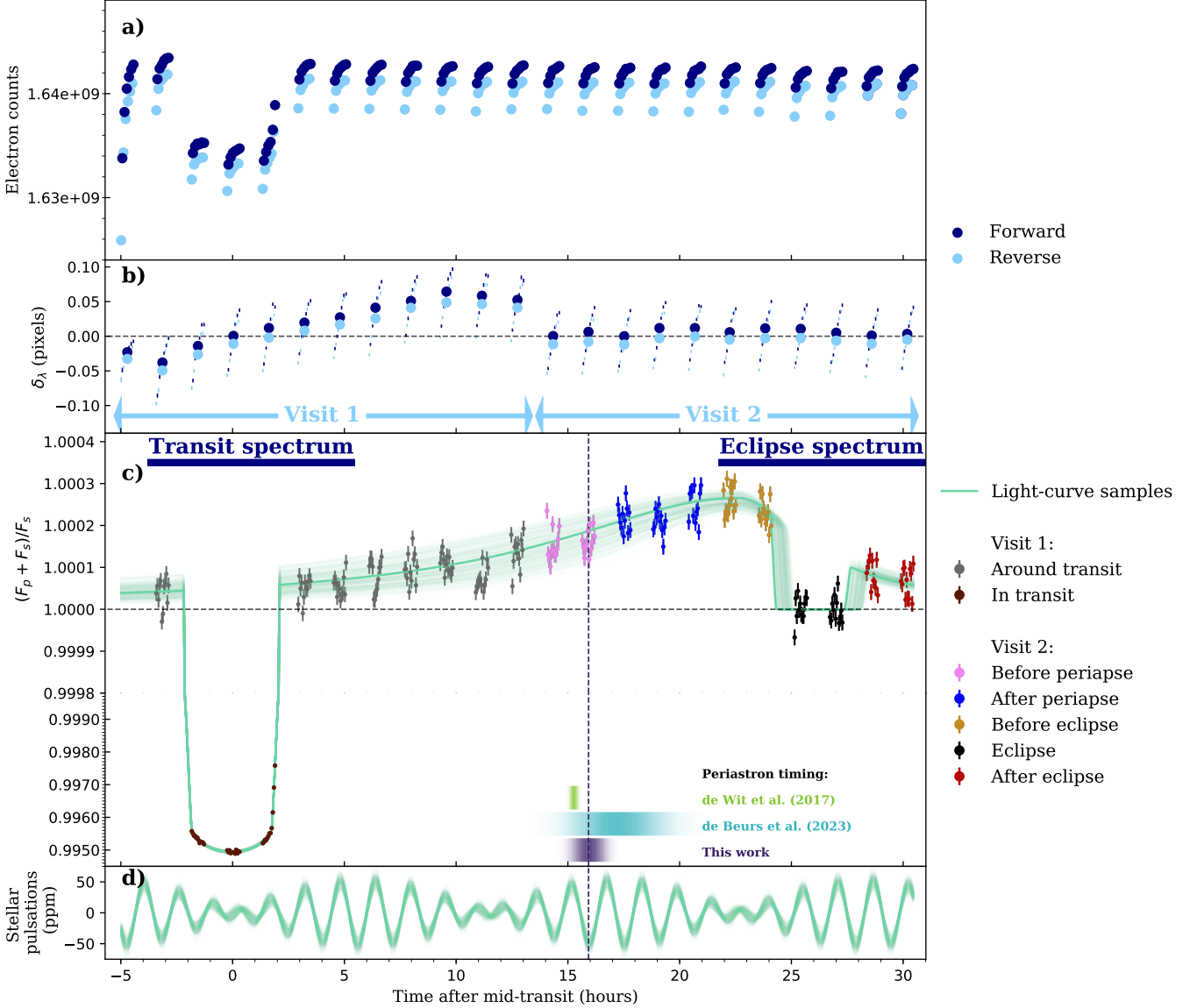


Figure 2. HAT-P-2b's WFC3 G141 light-curve starting just before transit and ending just after secondary eclipse.

a) Raw WFC3 G141 light-curve separated by scan direction. The flux levels of the two scan directions are different due to the upstream-downstream effect (McCullough & MacKenty 2012). Note that the first exposure of the penultimate orbit is missing: we omitted it because of a satellite crossing event.

b) Relative drift in pixels of each exposure on the WFC3 detector in the dispersion direction with respect to the reference exposure (δ_λ). Large dots mark the average over δ_λ for each orbit.

c) Telescope systematics-removed white light-curve data and best-fit planetary flux model ($\Phi(\mathbf{t}) + M(\mathbf{t})$) relative to the mean stellar flux. The first orbit has already been removed. The subsequent orbits have the same color coding as in Figure 1. We also show 200 posterior samples from the light-curve fits. We bolded the best-fit, which is pushed to an early eclipse by the priors. Note that the scale of the y-axis is different above and below $(F_p + F_s)/F_s = 0.9998$. For the white light-curve data we removed the best-fit telescope systematics. These are correlated with the planetary- and stellar fit parameters. Different light-curve posterior samples correspond to different telescope systematics and would they therefore alter the representation of the data in this figure slightly. We highlight the orbits that we used for the transit and eclipse spectra. In the bottom of this subfigure we plot the posterior distributions for the timing of periastron from de Wit et al. (2017), de Beurs et al. (2023), and this work. The median of the periastron posterior of this work is denoted with a vertical dashed line.

d) Stellar light-curve $\Psi(\mathbf{t})$ showing stellar pulsations from the 200 posterior samples shown in subfigure c. The scaling of this subplot is equal to the scaling of the upper part of subfigure c. The retrieved pulsation phases resemble the pulsation phases found in Spitzer data 5–9 years prior to these observations (de Wit et al. 2017).

ing Earth occultation starting with the eighth orbit until the fifteenth orbit of the observations presented in this work. Although HST did not take observations during the SAA crossing, the persistence of the elevated levels of cosmic rays may adversely affect the measured flux levels and the precision of the exposures taken after exiting the SAA in those orbits (Barker et al. 2009; Stevenson & Fowler 2019).

HST provides excellent pointing accuracy. But, for extended, multi-orbit observations, the telescope tends to drift $\sim 5 \text{ mas} \approx 0.04 \text{ pixels}$ during a 12-orbit visit (Stevenson & Fowler 2019). We cross-correlated the drop-off of the grism’s sensitivity curve for each exposure to the position of the drop-off in the reference exposure to find δ_λ , the band-integrated drift of the spectrum on the detector in the wavelength/dispersion direction. We show δ_λ in Figure 2b. There is a clear difference in alignment between the first visit and the second visit: the telescope drifted a total of $\sim 0.1 \text{ pixel}$ when averaged per orbit during the first visit, but it remained remarkably stable during the second visit. The measured intra-orbit drift may be due to telescopic breathing, rather than a genuine drift of the telescope. The root mean squared of δ_λ is 0.05 for the first visit and 0.03 for the second visit, both well inside the bounds defined by Stevenson & Fowler (2019) to be considered a successful observation.

2.2. White light-curve fitting

Figure 2a shows that time-dependent systematics dominate the WFC3 light-curve. They are strongest in the first orbit, which we therefore discarded. We modeled the flux $F(\mathbf{t})$ of the remaining data with:

$$F(\mathbf{t}) = T(\mathbf{t}) \times \Theta_{v,d}(\mathbf{t}) \times (\Phi(\mathbf{t}) + M(\mathbf{t}) \times \Psi(\mathbf{t})) \quad (1)$$

where \mathbf{t} is a vector of observation times, $T(\mathbf{t})$ models the orbit-long telescope systematics, $\Theta_{v,d}(\mathbf{t})$ models the visit-long telescope systematics, $\Phi(\mathbf{t})$ models the planetary phase curve, $M(\mathbf{t})$ models the planetary primary transit using batman (Kreidberg 2015a), and $\Psi(\mathbf{t})$ models the stellar light-curve. The subscripts v and d denote whether a parameter is a function of telescope visit, and scan direction respectively.

Firstly, we modeled the telescope systematics, $T(\mathbf{t})$, with the physically-motivated coupled differential equations from the RECTE charge trap model (Zhou et al. 2017). This requires four fit parameters: the number of initially filled fast/slow charge traps ($E_{f/s,0}$) and the number of fast/slow charge traps that are filled in between orbits ($\Delta E_{f/s}$). These parameters are shared between scan directions and visits. Having different RECTE parameters for the first and second visit does not improve the fits significantly.

Secondly, to model the visit-long telescope systematics we used a second-order polynomial for each visit separately:

$$\Theta_{v,d}(\mathbf{t}) = (f_{v,d} + V_{1,v,d}(\mathbf{t} - t_{f_v}) + V_{2,v,d}(\mathbf{t} - t_{f_v})^2) \times (1 + b \delta_\lambda) \quad (2)$$

where $f_{v,d}$ is a normalization constant, $V_{1,v,d}$ is a visit-long linear slope, $V_{2,v,d}$ is a visit-long second-order polynomial term, t_{f_v} is the time of the first exposure of the visit, b is a fit parameter and δ_λ is the band-integrated drift of the spectrum on the detector in the wavelength/dispersion direction seen in Figure 2b. We tested a model where we set $V_{2,v,d} = 0$ for either of the two visits, but this was disfavored by the Bayesian information criterion (BIC) for the white light-curve. Such model was disfavored for the first visit by $\Delta(\text{BIC}) = 314$ and it was disfavored for the second visit by $\Delta(\text{BIC}) = 39$. A model with a single unified second-order polynomial for both visits was disfavored by $\Delta(\text{BIC}) = 99$. A $\Delta(\text{BIC}) > 10$ is generally considered as very strong evidence and corresponds to a model preference of approximately 150:1 (Kass & Raftery 1995). This is a clear indication that the telescope systematics were different between the two visits.

Haynes et al. (2015) improved their WFC3 light-curve fits by correcting for the spectral drift in the wavelength direction, δ_λ . They did so by either shifting each exposure’s spectrum with respect to a reference spectrum during the data reduction phase of the analysis, or by decorrelating against δ_λ by adding an extra term $(1 + b \delta_\lambda)$ to their light-curve model (see also: Wakeford et al. 2016; Tsiaras et al. 2016; Barat et al. 2024). We chose the first method and performed it during our data reduction phase. However, despite that, we found that by additionally adding the extra b -parameter the BIC value of the full white light-curve fit improved by 71. A fit parameter to account for the shift of the spectrum in the spatial scan direction did not improve the fits. We note from Figure 2b that the repetitive intra-orbit shape of δ_λ resembles the hook-like pattern in Figure 2a. Also, a corner-corner plot of the posteriors (Figure 15 in Appendix B) shows clear correlations between b and the RECTE parameters. Therefore, the fit parameter b may, in fact, be tracing telescope breathing/charge trap systematics left uncorrected for by RECTE rather than a true dependence on the drift of the spectrum. Similarly, $V_{1,v,d}$ and $V_{2,v,d}$ may also be tracing a change in stellar brightness on a timescale longer than the duration of the telescope visits.

Thirdly, to model HAT-P-2b’s phase curve we followed de Wit et al. (2017) and used an asymmetric Lorentzian model:

$$\Phi(\mathbf{t}) = \begin{cases} 0 & \text{if: in eclipse} \\ F_p/F_{s,\min} + \frac{c_1}{u(\mathbf{t})^2 + 1} & \text{if: out eclipse} \end{cases} \quad (3)$$

$$u(\mathbf{t}) = \begin{cases} (\mathbf{t} - t_{\text{per}} - c_2)/c_3 & \text{if: } \mathbf{t} - t_{\text{per}} < c_2; \\ (\mathbf{t} - t_{\text{per}} - c_2)/c_4 & \text{if: } \mathbf{t} - t_{\text{per}} > c_2 \end{cases} \quad (4)$$

where $F_p/F_{s,\min}$ is the minimum flux of the phase curve, t_{per} is the time of periastron passage and c_1 , c_2 , c_3 , and c_4 are free parameters. c_1 is the maximum flux of the phase curve minus the minimum flux; c_2 is the difference in time between

periastron and the time of maximum flux; c_3 is the flux increase timescale; and c_4 is the flux decrease timescale. The timing of secondary eclipse and periastron passage are calculated from the planet’s orbital parameters with *batman*. We investigated using a phase curve model based on harmonics in orbital phase (Cowan & Agol 2008), like used by Lewis et al. (2013). Statistically, it provides a better fit than an asymmetric Lorentzian, but it creates a double humped light curve with its brightest peak during transit. We discard this harmonics-based fit as improbable.

Fourthly, the transit light-curve, $M(\mathbf{t})$, requires the input of HAT-P-2b’s orbital parameters. de Beurs et al. (2023) found hints that the eccentricity and argument of periastron may be significantly evolving, which matches what would be expected from stellar evolution models that incorporate tidal planet-star interactions (Bryan et al. 2024). We therefore plugged six fit parameters into *batman*: the planet’s radius in units of stellar radii, R_p/R_s ; the mid-transit time, t_0 ; the planet’s orbital inclination, i ; the orbital eccentricity, e ; its argument of periastron, ω_* ; the orbital semi-major axis in units of stellar radii, a/R_s ; and the linear limb-darkening coefficient u .

Lastly, to model the stellar light-curve, $\Psi(\mathbf{t})$, we used the two stellar pulsation modes discovered by de Wit et al. (2017):

$$\Psi(\mathbf{t}) = 1 + A_1 \cos\left(\frac{2\pi}{P_1}(\mathbf{t} - t_0 + \phi_1)\right) + A_2 \cos\left(\frac{2\pi}{P_2}(\mathbf{t} - t_0 + \phi_2)\right) \quad (5)$$

where $A_{1,2}$ are the pulsation amplitudes, $P_{1,2}$ the pulsation periods, and $\phi_{1,2}$ the pulsation phases. The WFC3 observations were made years after the Spitzer observations, rendering the priors from de Wit et al. (2017) uninformative for these WFC3 observations. We also fitted for $A_{1,2}$ and $\phi_{1,2}$, but we fixed $P_{1,2}$ to the fractions of the planet’s orbital period, P_{orb} , found by de Wit et al. (2017): $P_1 = \frac{1}{79}P_{\text{orb}} = 103$ min, and $P_2 = \frac{1}{91}P_{\text{orb}} = 89$ min. Coincidentally, the two pulsation periods found by de Wit et al. (2017) are extremely close to the orbital period of HST: ~ 96 min. This could cause some degeneracies between the pulsations and the orbit-long telescope systematics. Due to this, and because of the limited observed phase range, we did not search for other pulsation periods or modes. We gain confidence of including the two pulsation modes at these exact periods through the large difference in BIC that including the pulsations make: $\Delta\text{BIC} = 21$.

Without pulsations the transit depth would be 1.2σ deeper, the flux increase timescale, eclipse depths would be 2σ shallower, c_3 , would be 1.8σ shorter, and the flux decrease timescale, c_4 , would be 1.1σ longer.

2.3. Transit and eclipse spectra

To obtain transmission and eclipse spectra we split the G141 spectrum into 17 spectrophotometric bins that are 7-pixels wide and we fitted the spectral light-curves separately. We made sure that the most significant stellar line (hydrogen Paschen β at $1.282\mu\text{m}$) is fully encompassed by one bin and is therefore not split over multiple bins. This helps to decrease the impact of the drifting of the spectrum on the detector.

Because of the effects of the SAA and the enlarged uncertainties associated with fitting the full partial phase curve, we measured the transit and eclipse spectra by focusing on a subset of the observations: we used the one HST orbit preceding transit, the three in-transit orbits, and the two orbits following transit to determine the transit spectrum. For the eclipse spectrum we used the two orbits before eclipse, the two orbits in eclipse and the two orbits after eclipse. This is illustrated in Figure 2c.

We fitted the spectral light-curves with a similar model as the white light-curve fit described in the preceding section, but we fixed a number of parameters to the values found for the white light-curve: the orbital parameters, the spectral drift fit parameter b , the planetary light-curve parameters $F_p/F_{s,\text{min}}$, c_2 , c_3 , and c_4 , and the stellar pulsation parameters. This means that the only fit parameter left for the planetary light-curve (Equation 3) is the maximum flux, c_1 . We therefore kept $F_p/F_{s,\text{min}}$ at the value retrieved for the white light-curve. We obtained the secondary eclipse depth by evaluating Equation 3 at the time of secondary eclipse, t_{sec} . Because of the shorter baseline, we reduced the second-order polynomial visit-long baseline for the second visit to a linear baseline. The first visit still requires a second-order polynomial to properly describe the visit-long telescope systematics.

Despite the light-curve no longer being continuous, we kept $E_{f/s,0}$, $\Delta E_{f/s}$, and b shared between the transit and the eclipse data because we did not find any significant difference to these parameters between the visits. Sharing the telescope systematics parameters allows us to fit both data sets simultaneously to decrease the uncertainties on the telescope systematics and therefore increase the signal-to-noise ratio on the transit and eclipse depths. If we solely fit the secondary eclipse, the resulting spectrum differs from the combined fit by on average 0.5σ while the error bars are larger by 3%.

The stellar flux varies significantly between wavelengths, see Figure 3. Therefore, a different number of charge traps are filled at each wavelength, and the RECTE parameters are therefore required to be wavelength-dependent. In Table 2 we summarize the 25 fit parameters, the respective priors that were used for the white light-curve fit and their references (see Section 2.4). We also denote which eleven parameters are wavelength-dependent and therefore used for the 17 spectral fits. Because the divergence in measured amplitude between the stellar pulsations $1.1\text{-}1.7\mu\text{m}$ in this work and

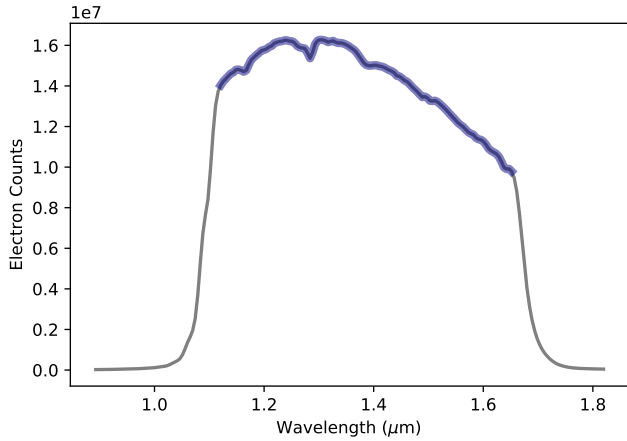


Figure 3. Average observed spectral stellar electron count rate per exposure during the occultation of HAT-P-2b. It is a convolution of the actual stellar spectrum and the G141 transmission function. The wavelengths that are used for this work are highlighted in blue. The observed count rate at the longest wavelength is only 60% of the peak count rate, requiring wavelength-dependent telescope systematics parameters.

4.5 μm in de Wit et al. (2017) is only modest, we assumed the pulsations to be monochromatic over the WFC3 G141 wavelength range.

2.4. Uncertainties and priors

In order to estimate the errors on the fitted parameters and identify the degeneracies in the model we used a Markov Chain Monte Carlo (MCMC) approach using the open-source emcee code (Foreman-Mackey et al. 2013). For the white light-curve fits, the chains have 30,000 steps with 250 walkers and a burn-in phase of 5000 steps. For the spectral fits, each chain has 10,000 steps with 110 walkers and a burn-in phase of 1000 steps. We test for convergence by averaging auto-correlation time over all walkers (Goodman & Weare 2010) and ensure that this is 50 times smaller than the number of samples.

Running an MCMC is computationally expensive, so minimizing the number of fit parameters is key. We therefore first ran a quick Levenberg-Marquardt fit (LM-fit; Newville et al. 2014) to get a good estimate of the best-fit parameters. We assumed that the LM-fit accurately determined the correct ratio between the visit-long telescope systematics of the two scan directions $V_{1/2,v,d}$, and we fixed that ratio. In the MCMC fit we then fitted for $\Delta V_{1/2,v}$, the difference with the value found by the LM-fit for the Forward scan direction, simplifying the light-curve fits. Furthermore, we also eliminated $f_{v,d}$ from the MCMC fits. $f_{v,d}$ provides an average electron level flux to RECTE. However, a relative difference in electron counts of less than a percent has an insignificant effect on the orbit-long ramp shape. We therefore deemed

the value of $f_{v,d}$ found by LM-fit good enough and simply renormalize the model to the data in the MCMC fits.

Literature-provided values serve as priors in the MCMCs for some parameters. de Wit et al. (2017) found the minimum Earth-facing, hemisphere-averaged temperature to be 1327 ± 106 K, which corresponds to $F_p/F_{s,\text{min}} = 9 \pm 5$ ppm at WFC3 G141 wavelengths. We doubled the uncertainty and used this as a prior on $F_p/F_{s,\text{min}}$, but we disallowed negative planetary fluxes.

The average final precision on the spectroscopic transit depths and eclipse depths are 49 ppm and 23 ppm respectively. This large difference in precision is largely caused by the requirement of a quadratic trend to model the telescope systematics in the first visit compared to a linear trend for the second visit ($V_{2,d} = 0$). A quadratic baseline has larger degeneracies with the transit depth. Also, the out-of-transit baseline is shorter than the out-of-eclipse baseline. Additionally, the RECTE parameters with regards to slowly trapped charges are mainly dependent on the pre- and in-transit orbits, adding extra degeneracies with the transit depth, but not to the eclipse depth. We reach an average precision of 6% and 8% above photon noise for transit and eclipse respectively.

In the light-curve fits we used four out-of-eclipse orbits. If we had used only two out-of-eclipse orbits and only fit for the eclipse light curve, the average precision on the eclipse spectrum would have decreased from 23 to 33 ppm. So, by doubling the out-of-eclipse baseline and observing a 6-orbit eclipse, we decreased the uncertainties by $\sim \sqrt{2}$, which is equivalent to observing a 4-orbit eclipse twice.

2.5. Partial phase curve

The most commonly used technique to remove telescope systematics from phase curves is to use a light-curve fitting method similar to the ones used in the previous sections (e.g. Stevenson et al. 2014; Kreidberg et al. 2018). Alternatively, the common-mode-based method developed by Arcangeli et al. (2021) allows us to extract the planetary spectrum at any orbital phase without fitting a light-curve. It would even allow us to extract the planetary spectrum if the light-curve were not continuous.

We give a short summary of the common-mode based method: one divides the spectral light-curve by the white light-curve. Subsequently one takes the in-eclipse spectrum as the stellar spectrum and divides all other spectra by this. We then grouped the data by HST orbits. This way, one can retrieve the planetary spectrum up to a monochromatic constant if the following restrictions are satisfied:

Firstly, the host star's spectrum should be invariable. The stellar pulsations found by de Wit et al. (2017) at 4.5 μm also seem to be present in these WFC3 data. However, we de-

Table 2. Sample priors and posteriors for the WFC3 light-curve fits of HAT-P-2b.

Parameter		Unit	Prior ^a	Posterior	Included in spectral fits?	Reference for prior
<i>Occultation depths</i>						
Transit depth	R_p^2/R_s^2	ppm	$\mathcal{U}(3500, 5500)$	4873 ± 9	✓	
Eclipse depth	$F_p/F_{s,sec}$	ppm	^b	141_{-15}^{+14}		
<i>Orbital parameters</i>						
Mid-transit time offset to [1]	Δt_0	min	$\mathcal{N}(0, 0.7469)$	2.44 ± 0.19		[1]
Orbital inclination	i	deg	$\mathcal{N}(86.16, 0.26)$	86.20 ± 0.13		[2]
Orbital eccentricity	e		$\mathcal{N}(0.50381, 0.0325)$	0.509 ± 0.005		[3]
Argument of periastron	ω_*	deg	$\mathcal{N}(194.7, 4.0)$	$191.6_{-2.0}^{+1.9}$		[3]
Scaled semi-major axis	a/R_s		$\mathcal{N}(9.04, 0.19)$	9.16 ± 0.15		[4]
Linear limb darkening parameter	u		$\mathcal{N}(0.297, 0.011)$	0.228 ± 0.004	✓	[5]
Time between mid-transit and periastron	t_{per}	hr	^b	15.9 ± 0.5		
<i>Planetary phase curve parameters</i>						
Minimum flux	$F_p/F_{s,min}$	ppm	$\mathcal{N}(9, 10)$	13_{-8}^{+10}		
Flux difference ($F_p/F_{s,max} - F_p/F_{s,min}$)	c_1	ppm	$\mathcal{U}(0, 10^5)$	245 ± 17	✓	
Peak flux delay from periastron	c_2	hr	$\mathcal{U}(0, 24)$	6.7 ± 0.6		
Flux increase timescale	c_3	hr	$\mathcal{U}(0, 14.4)$	$9.1_{-2.1}^{+3.4}$		
Flux decrease timescale	c_4	hr	$\mathcal{U}(0, 24)$	$3.9_{-0.6}^{+0.7}$		
<i>Telescope systematics</i>						
Initially filled slow charge traps	$E_{0,s}$	count	$\mathcal{U}(0, 1525.38)$	1261 ± 5	✓	[6]
Initially filled fast charge traps	$E_{0,f}$	count	$\mathcal{U}(0, 162.38)$	89.8 ± 1.3	✓	[6]
Extra filled slow charge traps in between orbits	ΔE_s	count	$\mathcal{U}(0, 1525.38)$	142.8 ± 2.6	✓	[6]
Extra filled fast charge traps in between orbits	ΔE_f	count	$\mathcal{U}(0, 162.38)$	91.1 ± 0.4	✓	[6]
Visit-long first polynomial term visit 1	$\Delta V_{1,c}$	ppm day ⁻¹	$\mathcal{U}(-3700, 3700)$	-100 ± 120	✓	
Visit-long first polynomial term visit 2	$\Delta V_{12,c}$	ppm day ⁻¹	$\mathcal{U}(-10000, 10000)$	-60_{-110}^{+130}	✓	
Visit-long second polynomial term visit 1	$\Delta V_{21,c}$	ppm day ⁻²	$\mathcal{U}(-8000, 8000)$	-140 ± 120	✓	
Visit-long second polynomial term visit 2	$\Delta V_{22,c}$	ppm day ⁻²	$\mathcal{U}(-2500, 2500)$	1070 ± 130		
Linear flux dependence on δ_λ	b	ppm pixel ⁻¹	$\mathcal{U}(-10^6, 10^6)$	1400 ± 160	✓	
<i>Stellar pulsation parameters</i>						
Amplitude pulsation mode 1	A_1	ppm	$\mathcal{U}(0, 105)$	23 ± 5		
Amplitude pulsation mode 2	A_2	ppm	$\mathcal{U}(0, 84)$	29 ± 5		
Phase pulsation mode 1 ^d	ϕ_1	hr	$\mathcal{U}(0, 1.71)$	0.99 ± 0.05		
Phase pulsation mode 2 ^d	ϕ_2	hr	$\mathcal{U}(0, 1.49)$	1.15 ± 0.04		

Notes.

^a The symbol \mathcal{U} is used to denote uniform priors and \mathcal{N} is used for Gaussian priors.

^b This parameter was not fit directly, but calculated from the other fit parameters. It is only shown here for reference

^c We fit for the difference with a second-order polynomial that was fit to the data prior to a run with an MCMC (see Section 2.4).

^d The pulsation phases were measured with respect to mid-transit.

References:

- [1]: [Ivshina & Winn \(2022\)](#)
[2]: [de Wit et al. \(2017\)](#)
[3]: [de Beurs et al. \(2023\)](#)
[4]: [Patel & Espinoza \(2022\)](#)
[5]: [Castelli & Kurucz \(2003\)](#); [Bourque et al. \(2021\)](#)
[6]: [Zhou et al. \(2017\)](#)

ected them to be largely of the same amplitude. The maximum difference in peak-to-trough pulsation amplitude between this work at $1.4\ \mu\text{m}$ and [de Wit et al. \(2017\)](#) at $4.5\ \mu\text{m}$ is 120 ppm at 3σ . The maximum color difference between the pulsation peaks and troughs is therefore $\sim 40\ \text{ppm}\ \mu\text{m}^{-1}$. We injected this spectral slope into our derived spectra and found that it alters the fitted temperature by 100 K, which is similar to the 1σ uncertainties on the fits themselves.

Secondly, the drift in pointing of the telescope must be sufficiently small, as this can alter the observed spectrum significantly. Figure 2b shows that the orbit-to-orbit variations of the drift of the spectrum are at most 0.1 pixels and 0.012 pixels for the first and second visit respectively. The spectral drift for the first visit is similar to the spectral drift for the transit visit in [Arcangeli et al. \(2021\)](#) which they found to be ill-suited for their common-mode method due to this spectral drift. The effect of the spectral drift for the second visit, however, is smaller than the spectral noise according to [Arcangeli et al. \(2021\)](#).

Thirdly, the long-term telescope systematics must be monochromatic. HST’s visit-long systematics are found to be wavelength-dependent (see e.g. [Kreidberg et al. 2014](#); [Stevenson et al. 2014](#); [Huber-Feely et al. 2022](#)). The telescope drift contributes to these systematics, but may not account for all. We tested this for the observations presented in this work by analyzing the wavelength-dependence of the visit-long polynomial coefficients, $V_{1,v,d}$ and $V_{2,d}$, in the transit and eclipse fits. These coefficients may account for both telescope systematics as well as star color variations. So, if these coefficients are wavelength independent, the first and third requirements for the common-mode method are simultaneously satisfied. However, we found that the single linear coefficient for the eclipse data, V_{1_2} is wavelength dependent by 2.6σ at $650\ \text{ppm}\ \text{day}^{-1}\ \mu\text{m}^{-1}$. This amounts to a possible 1800 K underestimate of a planetary blackbody temperature during the first orbit of the second visit. The first order polynomial term of the transit light curve is also wavelength dependent by 2.7σ . The caveat is that we analyzed the wavelength dependence of the visit-long trends using the transit and eclipse fits, which were only fit to a limited set of data (see Section 2.3). For the full white light-curve fits an extra polynomial order is required to accurately describe the second visit baseline. Also, the wavelength dependence of V_{1_2} may rather hint at inaccuracies in the modelling of the planetary phase curve in the transit-and-eclipse-only fits.

We therefore deem this common-mode method possibly applicable to the second visit, and unfit for the first visit because it violates the second and the third requirements.

In Section 2.1 we noted that we excluded the first exposure of the penultimate orbit because of the satellite crossing event. For the common-mode spectral reduction of this orbit, we therefore also omitted the first exposure of each in-eclipse

orbit, such that it is not biased by the wavelength dependence of HST’s orbit-long systematics. For all other orbits we continued to use all exposures.

3. ATMOSPHERIC MODELS

3.1. General Circulation models

We compare our observed WFC3 G141 white-light partial phase curve and phase-resolved spectra for HAT-P-2b with predictions from general circulation models (GCMs) presented in [Lewis et al. \(2014\)](#). These HAT-P-2b GCMs use the Substellar and Planetary Atmospheric Radiation and Circulation (SPARC) model ([Showman et al. 2009](#)) that employs the MITgcm ([Adcroft et al. 2004](#)) to treat the atmospheric dynamics and the non-gray radiative transfer model of [Marley & McKay \(1999\)](#), which has been applied in a wide variety of exoplanet atmospheric studies (e.g [Fortney et al. 2005](#); [Mayorga et al. 2019](#)). The HAT-P-2b GCMs consider atmospheric compositions of one times ($1\times$) and five times ($5\times$) solar metallicity both with and without TiO and VO. Chemical abundances are computed throughout the GCM grid assuming instantaneous thermochemical equilibrium given local temperature and pressure conditions ([Lodders & Fegley 2002](#); [Lodders 2003](#)). An intrinsic effective temperature (T_{int}) of 300 K and a pseudo-synchronous rotation period of 1.9462563 days is assumed for HAT-P-2b ([Lewis et al. 2014](#)).

Spectra as a function of orbital phase are produced from GCM outputs (temperature as a function of pressure along each column of the grid) that are recorded at regular intervals during the simulation. We track both the longitude of the substellar point and the longitude of an Earth observer throughout the simulation given the properties of HAT-P-2b’s orbit ([Kataria et al. 2013](#); [Lewis et al. 2014](#)). Emergent spectra from each of the GCM grid points on the hemisphere facing the Earth observer are calculated based on the local thermochemical structure and then averaged according to the methods presented in [Fortney et al. \(2006\)](#) to produce a single planetary emission spectrum as a function of orbital phase. These emission spectra are then convolved with the relevant instrument throughput function(s) to produce light curves and spectra as a function of planetary orbital phase and instrument bandpass.

3.2. 1D time-stepping models

We used EGP+ ([Mayorga et al. 2021](#)) to model both clear and cloudy atmospheres. EGP+ is a one-dimensional, time stepping, atmospheric model for planets on eccentric orbits. This model was built on the framework of the radiative-convective equilibrium models of [Marley & McKay \(1999\)](#); [Ackerman & Marley \(2001\)](#) and the time stepping evolution of [Robinson & Marley \(2014\)](#). Each model is initiated from apoastron and run for approximately 10 orbits to ensure con-

vergence to a quasi-periodic state under the assumptions of solar metallicity and C/O ratio. These models were run using the system parameters from Pál et al. (2010) and when applicable include MgSiO₃, MnS, Na₂S as condensates. We also run versions where we forcefully excluded TiO and VO, the primary agents for thermal inversions.

3.3. 1D free-chemistry models

We used the open-source atmospheric retrieval package POSEIDON (MacDonald & Madhusudhan 2017; MacDonald 2023; Coulombe et al. 2023) to infer the temperature structure and chemical composition of the atmosphere at each orbital phase. For this analysis, we used a temperature-pressure (TP) profile designed for brown dwarfs (Piette & Madhusudhan 2020), but modified it to allow for negative temperature gradients (thermal inversions). The free parameters of this temperature model are the atmospheric temperature at 1 bar pressure and temperature gradients between the following pressure nodes: 10⁻⁵, 10⁻³, 10⁻¹, 10¹, and 10² bar. The priors on the temperature differences between the parameterized layers are -1000 – 1000 K except between the deepest layers, which is uniform between 0 – 1000 K as we expect the deep atmosphere to be non-inverted. The prior on the temperature at 1 bar is uniform between 400 – 4000 K. We include the following opacity sources: H₂-H₂ and H₂-He collision-induced absorption (Karman et al. 2019), H₂O (Polyansky et al. 2018), H⁻ (John 1988), FeH (Wende et al. 2010), TiO (McKemmish et al. 2019), and VO (McKemmish et al. 2016). We fit for constant-with-pressure volume mixing ratios in log space for each of the chemical species, with uniform priors between -12 – -1, and assume the remainder of the atmosphere is H₂ and He at the solar ratio. Finally, we fit for the planet’s radius at 10⁻² bar and a constant offset on the spectra (phase-curve spectra only), both constrained by Gaussian priors from the white-light analysis.

We calculate emission spectra using opacity sampling at a resolution of $R = 10,000$. Our model has 100 pressure layers from 10⁻⁵ – 10² bar. For the stellar spectrum, we use a PHOENIX model (Husser et al. 2013) assuming a stellar radius of 1.64 R_{\odot} , an effective surface temperature of 6414 K, a metallicity of 0.04, and a surface gravity of $\log(g) = 4.18$ (Pál et al. 2010; Tsantaki et al. 2014) interpolated with pyMSG (Townsend & Lopez 2023). We explore the parameter space with PyMultiNest, a Python extension of MultiNest (Feroz et al. 2009; Buchner et al. 2014) using 1,000 live points.

4. RESULTS ON THE LIGHT-CURVE FITS

We display the best-fit white light-curve as well as 200 posterior samples for the planetary light-curve in Figure 2c and for the stellar light-curve in Figure 2d. In Table 2 we list these posteriors for all the fit parameters.

Notable in the white light-curve data of Figure 2c is that the flux of the penultimate orbit of the first visit seems to be anomalously low compared to the best-fit light-curve. Before the data of this orbit were taken, the telescope experienced the strongest SAA crossing of the entire observation. The penultimate orbit of the first visit is therefore likely most impacted by the negative effects from the SAA described in Section 2.1. We tested omitting this orbit from the fits, but that does not change the posteriors of any fit parameters at more than 1 σ . We note that the SAA may have affected more orbits than just the penultimate orbit of the first visit, albeit less visibly.

4.1. Orbital parameters

In Figure 4 we show a corner-corner plot between the most important retrieved orbital parameters and we compare them to literature values from de Wit et al. (2017) and Ivshina & Winn (2022). We also include predictions from the model by de Beurs et al. (2023). We measured an eccentricity of $e = 0.509 \pm 0.005$ and an argument of periastron $\omega_{\star} = 191.6^{+1.9}_{-2.0}$ degrees. The first is consistent $\leq 1\sigma$ with previous works, while ω_{\star} is 1.6 σ larger.

We found the transit to occur at $t_0 = 2459204.11219 \pm 0.00014$ BJD TDB, which is discrepant with Ivshina & Winn (2022) at 3.3 σ . This difference is potentially due to the tidal star-planet interactions.

From the posteriors of Δt_0 , e , and ω_{\star} , we calculated the time of secondary eclipse to be $t_{\text{sec}} = 2459205.2094 \pm 0.012$ BJD TDB and the time of periastron to be $t_{\text{per}} = 15.9 \pm 0.5$ hr after the primary transit. The precision on t_{sec} is much lower than on t_0 because we did not clearly detect the ingress or egress of the secondary eclipse. The time between periastron and the primary transit was 0.67 ± 0.5 hr longer than in the epoch de Wit et al. (2017) observed (2011-2015) and consistent with the predictions from de Beurs et al. (2023) for this epoch (December 2020).

4.2. Stellar pulsations

We included two stellar pulsation modes. The amplitudes we measure, without having put priors on them, are 23 ± 5 ppm and 29 ± 5 ppm: which respectively corresponds to 0.66 ± 0.14 and $1.02^{+0.16}_{-0.17}$ times the amplitudes found by de Wit et al. (2017) at 4.5 μm . Also, the pulsation phases are very similar to those in de Wit et al. (2017): the pulsation modes interfere destructively during transit and constructively during eclipse.

4.3. Planetary phase curve parameters

We present the posteriors of the phase curve fit parameters in Figure 5. We found a peak F_p/F_s of 258 ± 14 ppm about $c_2 = 6.7 \pm 0.6$ hr after periastron passage and $F_p/F_{s,\text{min}} = 13^{+10}_{-8}$ ppm. This corresponds to Earth-facing, hemisphere-averaged planetary brightness temperatures of 2360 ± 30 K

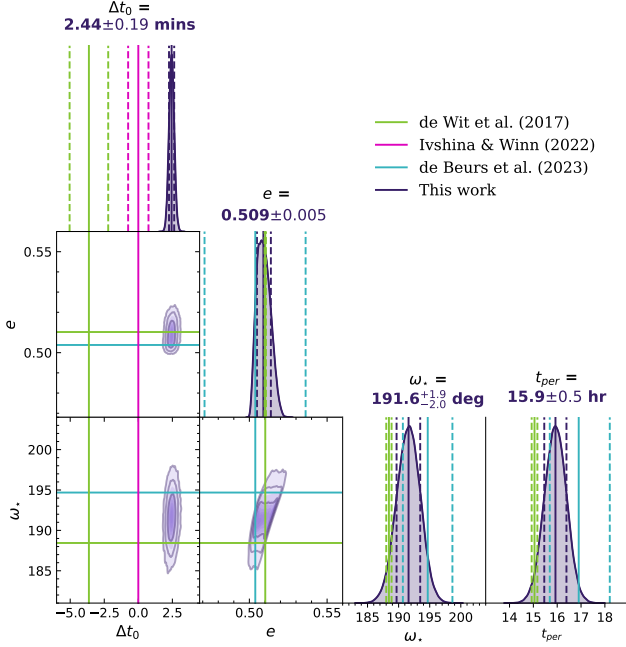


Figure 4. Corner-corner plot of HAT-P-2b’s orbital parameters from the white light-curve fits. This is an excerpt from the full corner-corner plot in Figure 15 in Appendix B. From left to right: Δt_0 , the difference in minutes between the measured transit and the predicted timing of mid-transit from Ivshina & Winn (2022); e , the orbital eccentricity; ω_* , the argument of periastron; and t_{per} , the difference in hours between t_0 and the time of periastron that is derived from the measured t_0 , e , and ω_* . Because t_{per} is almost uniquely defined by ω_* , we do not show its correlations. Median values are denoted with a solid line in the histograms and 1σ values are denoted with dashed lines. We overplot the values found by de Wit et al. (2017) (green), Ivshina & Winn (2022) (brown) and de Beurs et al. (2023) (blue).

and 1390_{-160}^{+120} K respectively. Our measurements find a timescale for planetary flux increase $c_3 = 9.1_{-2.1}^{+3.4}$, and a much shorter timescale for planetary flux decrease $c_4 = 3.9_{-0.6}^{+0.7}$ hr.

We compare our results against the 3D GCMs as well as the 1D time-stepping models in Figure 6. Until secondary eclipse the flux is higher than the flux modeled by the GCMs, but after eclipse the flux is overestimated by the 1D model. Unlike at $4.5\ \mu\text{m}$, the differences in expected flux between the versions of the two types of forward models is not large enough to make a significant distinction between them. The differences between the cloudy and cloudless models are small because the modeled cloud layers are deeper than the WFC3 photosphere.

A crucial difference between the two categories of forward models lies in the flux decrease timescale. In the GCMs the flux decreases on a timescale of ~ 8 hours, and in the 1D time-stepping models it decreases in ~ 17 hours. The difference between the two types of forward models is largely rooted in their treatment of advection and the inherent three-

dimensional nature of the planet. Contrary to the atmospheric columns modeled by the GCMs, the 1D time-stepping models have no neighboring columns for which to calculate the mutual exchange of heat. As such, the 1D time-stepping models do not consider horizontal advection. Also, the flux shown in Figure 6 for the 1D time-stepping model is the calculated flux of the dayside rather than the Earth-facing hemisphere. Between periastron and secondary eclipse this is a decent approximation since the flux emanating from the Earth-facing hemisphere is dayside-dominated at those times. However, accounting for rotation and therefore the visible fraction of the dayside, would decrease the flux increase/decrease timescales and bring them more in line with the 3D GCMs and the observed flux.

4.4. Transit and eclipse spectra

In Figure 7 we exhibit the WFC3 transmission spectrum. The atmospheric scale height during transit is approximately 24 km given a temperature of 1300 K and a mean molecular mass of 2.33 (Lewis et al. 2014). This corresponds to 3 ppm in terms of R_p^2/R_s^2 , the transit depth. Because the mean spectral uncertainty for the transit spectrum is 49 ppm we can draw no conclusions on the atmospheric condition during transit. This notion is corroborated by the forward 1D equilibrium chemistry models. Indeed, the WFC3 spectrum has no detected slope within 0.5σ . However, its reduced χ^2 is 1.8, indicating that the scatter is larger than expected, largely due to the telescope systematics (δ_λ).

As the planet transits in front of the star, its nightside is visible to the observer, carrying an imprint on the transmission spectrum. Due to the nature of the fitting method used for the transit data, we are insensitive to the nightside flux itself and we can only measure its variation. From the fitted light-curve we estimate that, during transit, the planet’s Earth-facing brightness temperature increased by ~ 30 K, introducing a potential slope of $\sim 10\ \text{ppm}\ \mu\text{m}^{-1}$. This is much smaller than the measured uncertainty on this slope of $40\ \text{ppm}\ \mu\text{m}^{-1}$. Changes in spectral features would be even smaller. Planetary nightside flux variations during transit can therefore safely be ignored for the transmission spectrum.

Because the expected spectral transmission features are so small, we assume the spectrum to be featureless. WFC3’s precision therefore allows us to improve the precision on the relative planetary radius by a factor 3 with respect to the previous measurement by de Wit et al. (2017). At transit we measure a WFC3 weighted average planetary radius over stellar radius of $R_p^2/R_s^2 = 0.004869 \pm 0.000012$.

Figure 8 displays the secondary eclipse spectrum from the WFC3 data augmented with the Spitzer data from Lewis et al. (2013) (3.6 and $8.0\ \mu\text{m}$) and from de Wit et al. (2017) ($4.5\ \mu\text{m}$). These data, and likewise the spectral transit depths, are listed as well in Table 5 in Appendix B. One should use

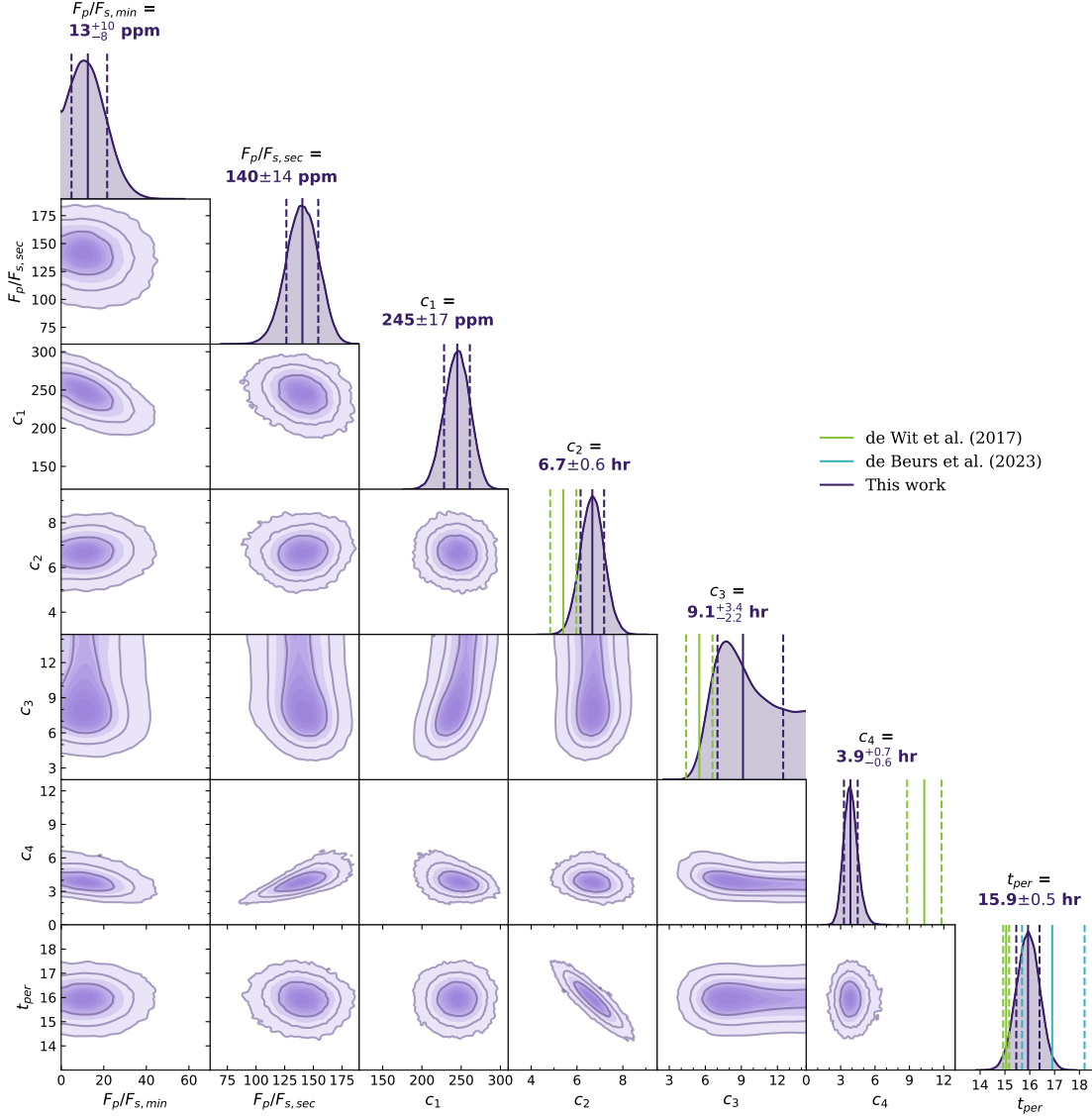


Figure 5. Corner-corner plot of HAT-P-2b’s phase curve parameters from the full light-curve fits. Correlations between the fit parameters shown in this Figure and other fit parameters are shown in Figure 15 in Appendix B. From left to right: $F_p/F_{s,min}$, the minimum planetary flux in ppm; $F_p/F_{s,sec}$, the secondary eclipse depth in ppm, which is not fit but derived from the other parameters; c_1 , the difference in planetary flux between its minimum and maximum in ppm; c_2 , the difference in hours between periastron and the time of flux maximum; c_3 , the flux increase timescale in hours; c_4 , the flux decrease timescale in hours; and t_{per} , the difference in hours between t_0 and the time of periastron. We overplot the values found by de Wit et al. (2017) (green), and de Beurs et al. (2023) (blue). Median values are denoted with a solid line in the histograms and 1σ uncertainties are denoted with dashed lines.

caution when comparing the eclipse depths of this work to literature values, because they were taken at different epochs. Therefore, they were taken with different observing geometries, and consequently with different eclipse timings compared to periape, and therefore a different expected temperature. We excluded the Spitzer data at $5.8\mu\text{m}$ from Lewis et al. (2013) because eclipse measurements at those wavelengths are often found to be less reliable because of the differing telescope characteristics (Désert et al. 2009; Stevenson et al. 2010; Désert et al. 2011; Lewis et al. 2013).

We also added forward spectral models from the 3D GCMs and the 1D time-stepping models to Figure 8. Due to the different expected temperatures (see Figure 6), it is difficult to directly compare the models to the data. However, the shape of the WFC3 eclipse spectrum most closely resembles either a blackbody spectrum, or a spectrum without TiO/VO.

The lower panel of Figure 8 compares the HAT-P-2b WFC3 spectrum eclipse spectrum from the RECTE method (purple) to the common-mode reduced spectrum (grey). For the common-mode based spectrum we used the same orbits as for the RECTE fit and we added a monochromatic constant

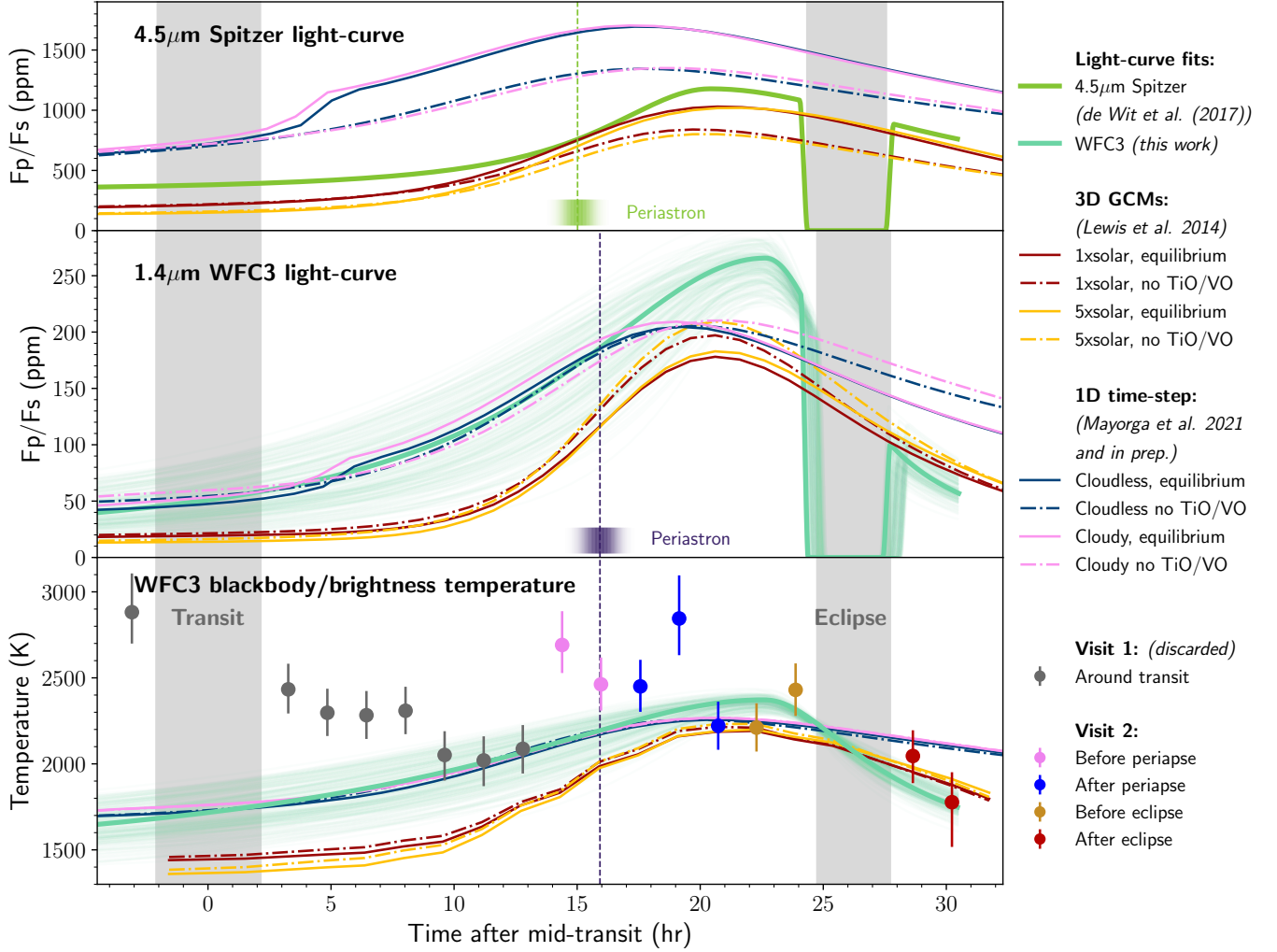


Figure 6. HAT-P-2b’s partial phase curve compared to a suite of forward models. We denote the 3D GCMs by Lewis et al. (2014) in red for the solar metallicity case and in yellow for the 5×solar metallicity case. Cloudless 1D solar metallicity forward models by (Mayorga et al. 2021, and in prep.) are blue and cloudy models are pink. For the models we denote the equilibrium case with a solid line and cases where TiO and VO are excluded with a dash-dotted line. We also denote the posterior distribution of the time of periastron from this work (purple) and from de Wit et al. (2017) and we show their median as a dashed line. The 1D time-stepping forward models are for the planet’s dayside rather than the Earth-facing hemisphere. Between periastron and secondary eclipse this is a decent approximation.

Upper: Planetary flux relative to the stellar flux at Spitzer’s 4.5 μm wavelengths from de Wit et al. (2017) in green. The models are sampled at the epoch, and therefore orbital geometry, at which de Wit et al. (2017) observed. The 1D time-step show a sudden step in brightness at ~5 hours after mid-transit due to the sudden onset of a thermal inversion and therefore a sudden change in atmospheric layers probed.

Middle: F_p/F_s at WFC3 wavelengths. 200 posterior samples from Figure 2 are shown in aquamarine green with the best-fit light-curve being bolded. The models are sampled at the epoch of the WFC3 observations.

Lower: Common-mode blackbody temperature phase curve compared to modeled blackbody temperatures and brightness temperatures of the white light-curve fits. The measured temperatures were calculated for each orbit using the common-mode method and a blackbody fit. We converted the F_p/F_s from the models to blackbody temperatures by fitting a blackbody to their phase-resolved spectra, hence why the GCM temperatures are more bumpy than the modeled band-averaged flux. The common-mode measured temperatures of the second visit are also noted in Table 4. We discard the common-mode results for the first visit because of the strong telescope systematics as discussed in Section 2.5.

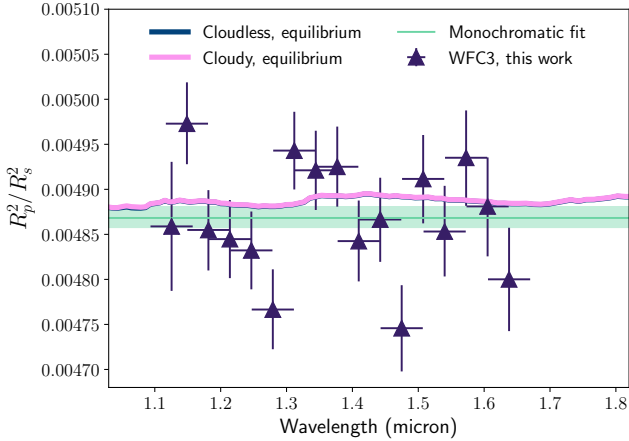


Figure 7. HAT-P-2b’s transmission spectrum measured for WFC3. We overplot the monochromatic fit (aquamarine green) as well as cloudless (blue) and cloudy (pink) 1D equilibrium chemistry models from Section 3.2. The shaded region on the fit denotes a 1σ uncertainty on the wavelength-averaged transit depth. Because the clouds in the cloudy model reside at very high pressures, the cloudless and cloudy models are so similar that they are almost indistinguishable in this plot.

such that the means of both spectra are the same. Despite a visible difference in slope, the two spectra are in decent agreement with each other and differ by at most 0.8σ . We stress here that these methods are based on completely different principles, yet they produce a similar spectrum. This is a testament to the possibilities that the common-mode based method by Arcangeli et al. (2021) creates.

The F_p/F_s of the RECTE method in the spectral bin centered at $1.28\mu\text{m}$ is 2.4σ higher than the blackbody fit and it does not coincide with any spectral features in the models. By itself, such deviation does not warrant this bin to be flagged as anomalous, but the deviation is also visible throughout the partial phase curve (see Section 5.3). We therefore exclude this bin from the spectral retrievals and discuss its origin in Section 6.4. Excluding this spectral bin, a blackbody fits the WFC3 data at $\chi^2_\nu = 0.83$.

In Appendix A we compare the transmission and eclipse spectra to those found by Changeat et al. (2022) and Edwards et al. (2023).

4.5. Spectral retrievals

We used the 1D free-chemistry retrievals outlined in Section 3.3 to chemically and thermally characterize HAT-P-2b’s atmosphere during eclipse. The resulting best-fit is depicted in aquamarine green in Figure 8 with the corresponding corner-corner plot shown in Figure 16 in the Appendix. In Figure 9 we plot the best-fit TP-profile with the corresponding contribution function. It is notable that the median TP-profile looks nearly isothermal, while the best-fit model is not. This indicates multiple possible solutions to the spec-

trum. The contribution function of the best-fit model indicates that we probe lower pressures than the forward models predict. Contrary to the expectations based on the spectra of the forward models, we retrieve a high median H^- abundance of $\log(\text{H}^-) = -4.0^{+2.3}_{-5.4}$ while the TiO and H_2O abundances are largely unconstrained within our priors.

The $1.28\mu\text{m}$ bin not only coincides with the Pa β line, but it is also close to the peak of a TiO opacity band. Therefore, if the $1.28\mu\text{m}$ bin had been included in the fits, the TiO volume mixing ratio would run up against the edge of the prior, although low TiO abundances are not excluded.

In order to test and quantify the significance of the presence of the molecules detected in the secondary eclipse spectrum, we ran identical retrievals with each molecular opacity source removed. By comparing the Bayesian evidences, we calculate an equivalent detection significance of each molecule. We list the results in Table 3 and we conclude that the presence of TiO and H_2O are the most significant at 1.5σ . However, neither makes the 3σ threshold to qualify for a detection.

5. PHASE-RESOLVED SPECTRA RESULTS

5.1. Blackbody temperature fits

To investigate the evolution of HAT-P-2b’s spectrum throughout its orbit, we utilized the common-mode method discussed in Section 2.5. We fitted a blackbody model to the spectra using an MCMC method (Foreman-Mackey et al. 2013) to retrieve a phase-resolved blackbody temperature. Importantly, the common-mode method produces planetary emission spectra that are only *relative* up to a monochromatic constant. We therefore added a monochromatic constant to fits of the common-mode spectra. We used a PHOENIX stellar model for HAT-P-2 (Husser et al. 2013), and we again excluded the wavelength bin centered around $1.28\mu\text{m}$.

We present the retrieved blackbody temperatures in Figure 6 and compare them to a brightness temperature curve derived from the white light-curve fits by multiplying them with a PHOENIX stellar models (Husser et al. 2013). In order to also properly compare the performance of the common-mode method to the predictions, we fit a blackbody to the 3D and 1D model spectra at WFC3 wavelengths for each time stamp. The forward models show a significantly lower planetary temperature, especially for the planet’s nightside during transit. Close to secondary eclipse, the retrieved temperatures align very well with the 3D models and the light-curve-derived temperature curve, but earlier orbits stray away from them. In the blackbody fits to the forward models we did not fit for any monochromatic offset. Including such offset would significantly decrease the modeled blackbody temperature, further increasing the difference with the data.

Noticeably, there is a clear step between the first and second visit. We emphasize that the common-mode based

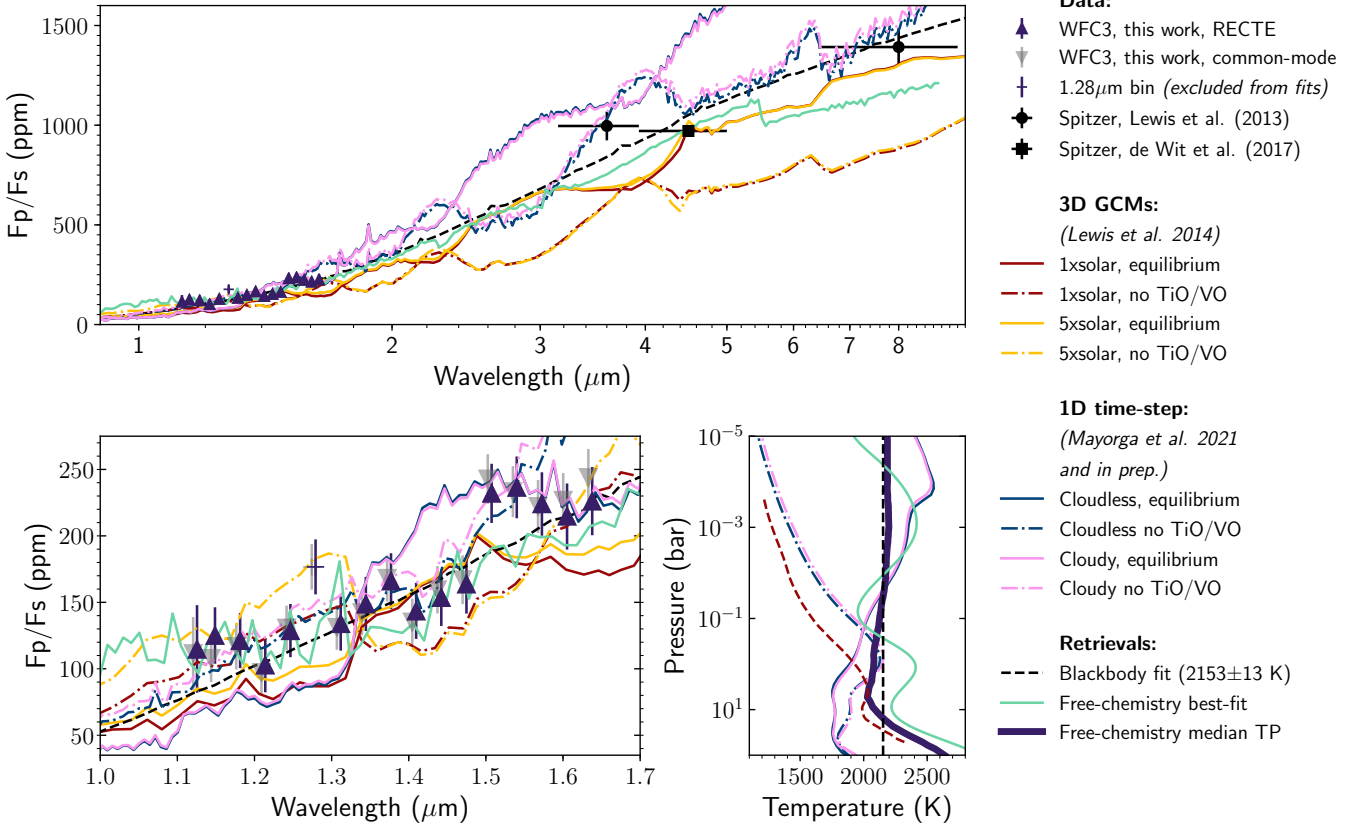


Figure 8. HAT-P-2b’s eclipse spectrum for WFC3 with the RECTE fit (purple), with the common-mode method (grey) and for the Spitzer observations (black) (Lewis et al. 2013; de Wit et al. 2017). We also overplot a blackbody fit (dashed black line), the 3D GCM models (red, yellow), the 1D time-stepping models (blue, pink), and the best-fit 1D free-chemistry retrieval (aquamarine green). The retrieval was performed on the WFC3 data only, but excluding the bin centered at $1.28\ \mu\text{m}$ (denoted with a cross). See Section 5.3 for a discussion on this.

Upper: Full HAT-P-2b near-infrared eclipse spectrum. We sampled the forward models at what was the time of secondary eclipse during the epoch of the Spitzer observations (2011). This makes for a ~ 80 ppm difference at Spitzer wavelengths compared to the WFC3 epoch (2020). The Spitzer data by Lewis et al. (2013) do not take any stellar pulsations into account.

Lower left: Eclipse spectrum zoomed in on the WFC3 wavelengths. The models are sampled at the epoch of the WFC3 observations (2020). We added a monochromatic offset to the common-mode reduced spectrum to match the average eclipse depth of the RECTE fit. We also offset the common-mode reduced spectrum in wavelength slightly to make it more distinguishable from the RECTE fit. Note that the common-mode method is entirely different from the RECTE method, yet the results are relatively similar.

Lower right: Temperature pressure profiles of the models, sampled at the time of secondary eclipse during the WFC3 epoch. The equilibrium forward models have a thermal inversion, while the models without TiO/VO do not. The median TP-profile (purple) of the free-chemistry retrieval is almost isothermal, while the best-fit profile (aquamarine green) is not.

method investigates the spectrum of an HST orbit with respect to the spectrum in secondary eclipse. Therefore, the more similar the telescope systematics and stellar spectrum are to those in eclipse, the more accurate the observed planetary phase-resolved spectra will be. In Section 2.5 we established that the telescope systematics are too large for the first visit, but possibly acceptable for the second visit. Henceforth we will concentrate on the phase-resolved spectra of the second visit and ignore the first visit’s phase-resolved spectra. We tried recovering useful spectra from the first visit by dividing those spectra by the two orbits just after transit instead of the orbits in eclipse. However, those first-visit common-mode-reduced spectra still showed significant sys-

tematics and their slopes were either too steep (indicating an extremely hot planet), or negative.

We suggested in Section 2.5 that existing telescope systematics and/or stellar effects may result in the planetary temperature during the first orbit of the second visit to be underestimated by ~ 1800 K. We find the contrary: the measured temperatures at the start of the second visit are higher than expected.

Table 4 lists the retrieved blackbody temperatures and offsets, and Figure 10 shows the phase-resolved spectra and the blackbody spectra. We combined the orbits into four groups: the two orbits before periastron (pink), the three orbits just after periastron (blue), the two orbits just before

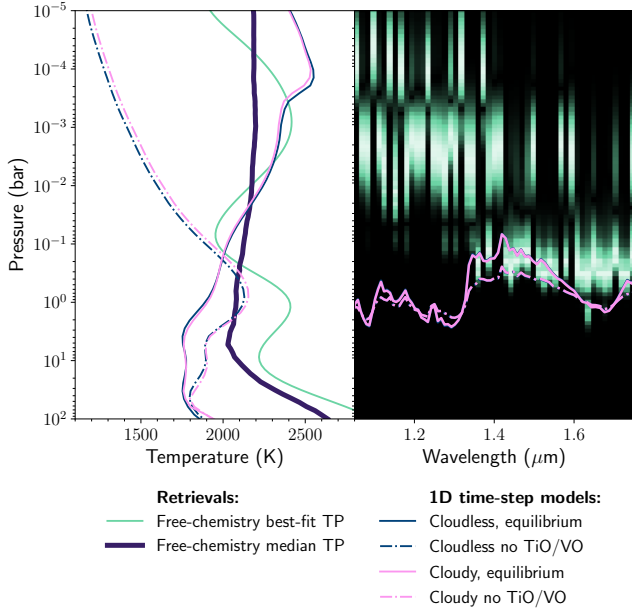


Figure 9. Best-fit (aquamarine green) and median (purple) temperature pressure (TP) profiles of the 1D free-chemistry retrievals of the secondary eclipse spectrum. The panel on the right displays the contribution function that corresponds to the best-fit TP-profile. We compare this to the TP-profiles and the pressure of the $\tau = 0.5$ layer of the 1D time-stepping forward models. There are almost no differences between the cloudy and cloudless contribution functions.

eclipse (gold) and the two orbits after eclipse (red). We also show blackbody fits with priors on the monochromatic offset. We utilized the posterior distribution of F_p/F_s from the white light-curve fit as a prior on the monochromatic offset. These blackbody fits show that slightly more sensible results can be obtained if the light-curve is known. However, they are still very different from the forward models around periapse.

Figures 10, 11 and Table 4 suggests that the spectral temperature declines throughout the visit, albeit not significantly until after secondary eclipse. In Section 5.4 we assess what the stellar contribution to this decline could be.

The spectral structure observed in the eclipse spectrum in Section 4.4 is also visible in the phase-resolved spectra in Figure 10, indicating that the chemistry of the planet’s atmosphere at the pressures probed by this observation did not change significantly throughout this phase of the planetary orbit. Moreover, the spectral bin at $1.28 \mu\text{m}$ is consistently more than 1σ above the blackbody fit. We further discuss this feature in Section 5.3.

5.2. Spectral retrievals

In Section 4.5 we performed 1D free-chemistry retrievals on the secondary eclipse spectrum. We performed similar retrievals on the partial-phase curve spectra, again excluding the bin at $1.28 \mu\text{m}$. However, due to the nature of the

common-mode method, we added an extra parameter to fit for the monochromatic offset. We again leveraged the posterior distribution of F_p/F_s from the white light-curve fit as a prior to the offset. In Figure 10 we plot the retrieved spectra as aquamarine green lines. In Table 3 we provide the retrieved volume mixing ratios and the statistical significance of the detection of each molecule. In Figure 17 in the Appendix we plot the contribution functions corresponding to the best fits.

The median retrieved temperature-pressure (TP) profiles shown in Figure 11 show an evident temporal structure: the first observed phase (before periapse) has a significant thermal inversion. The disappearance of this inversion, and the hotter WFC3 photosphere after periapse would suggest that heat is deposited further down in the atmosphere. As the planet recedes further from its host star, it cools down, until after eclipse the photospheric temperature drops below 2000 K. However, it is important to note that the retrieved WFC3 photospheric temperature is strongly driven by the priors on the monochromatic offset. As such, the significance of Figure 11 is in the vertical thermal structure rather than the absolute temperature.

The need for an extra opacity in the before-periapse spectrum is evident from the large difference between the blackbody fit without priors and the forward models in Figure 10. The fit without priors effectively probes the slope of the spectrum, which is steeper than expected from the brightness temperature of the forward models. Therefore, an extra opacity source that has a strongly positive slope throughout the WFC3 spectrum is necessary to bring down the retrieved temperature. H^- in absorption with a temperature that decreases steeply with altitude, between $10^{-3} - 10^{-5}$ bar fits this bill. However, this also requires the layers below the WFC3 photosphere to be inverted. This provides a window into deeper, cooler layers, that could fit the relatively cool redmost data point. However, none of that is predicted by the forward models, nor has H^- in absorption been predicted by any GCMs (Parmentier et al. 2018). Alternatively, TiO in absorption with an unrealistically high $\log(\text{VMR}) \approx -2$ may also explain this spectrum, but struggles to fit for the redmost data point.

As such, the retrieved abundances strongly depend on the slope of the spectra. However, the accuracy of these slopes remains uncertain (see Figure 6 and Sections 2.5, 5.1, and 5.4).

5.3. Significant deviation from a blackbody at $1.28 \mu\text{m}$

Figure 10 shows that the wavelength bin centered around $1.28 \mu\text{m}$ has an anomalously high flux compared to blackbody fits throughout the entire second visit. This bin wholly contains the strong stellar Paschen β line at $1.282 \mu\text{m}$, which arises from the electronic transition within hydrogen atoms

Phase	H ₂ O			TiO			VO			H ⁻			FeH		
	log(X_i)	\mathcal{B}	Sign.												
Before periapse	-6.8 ^{+3.3} _{-3.2}	0.8	1.0 σ	-6.5 ^{+3.3} _{-3.4}	1.1	1.1 σ	-6.5 ^{+3.1} _{-3.4}	0.9	0.9 σ	-4.2 ^{+0.4} _{-1.6}	4.5	2.3 σ	-5.6 ^{+2.8} _{-3.8}	1.3	1.5 σ
After periapse	-6.3 ^{+3.5} _{-3.5}	1.0	1.1 σ	-5.3 ^{+2.7} _{-4.0}	1.2	1.4 σ	-3.0 ^{+0.8} _{-4.9}	0.8	1.0 σ	-6.5 ^{+2.5} _{-3.2}	0.6	1.1 σ	-6.6 ^{+3.0} _{-3.2}	1.0	0.9 σ
Before eclipse	-6.0 ^{+3.6} _{-3.5}	1.3	1.4 σ	-5.7 ^{+3.7} _{-3.7}	1.0	0.9 σ	-6.1 ^{+3.3} _{-3.5}	0.9	0.9 σ	-4.5 ^{+2.6} _{-5.0}	0.5	1.2 σ	-5.2 ^{+2.6} _{-3.8}	1.5	1.6 σ
Secondary eclipse	-5.8 ^{+3.5} _{-3.9}	1.3	1.5 σ	-6.2 ^{+3.1} _{-3.3}	1.4	1.5 σ	-6.8 ^{+3.5} _{-3.1}	1.2	1.3 σ	-4.0 ^{+2.3} _{-5.4}	0.9	0.9 σ	-5.0 ^{+2.7} _{-4.0}	1.2	1.3 σ
After eclipse	-6.1 ^{+3.4} _{-3.5}	1.1	1.3 σ	-6.5 ^{+3.3} _{-3.3}	1.1	1.2 σ	-6.6 ^{+3.4} _{-3.4}	1.2	1.3 σ	-4.6 ^{+2.7} _{-4.8}	1.1	1.2 σ	-5.5 ^{+3.0} _{-3.7}	1.1	1.3 σ

Table 3. Chemistry results of the 1D free-chemistry retrievals. For each molecule and for each partial-phase curve spectrum we list the volume mixing ratio ($\log(X_i)$), the Bayes factor \mathcal{B} between a model with and without that molecule, as well as the equivalent statistical significance of the detection of that molecule.

Phase	BB Temperature	Blackbody fits						Free-chemistry retrieval fit	
		Grouped BB temperature		Constant offset (ppm)		χ^2_v		Constant offset (ppm)	χ^2_v
		no prior	with prior	no prior	with prior	no prior	with prior		
0.106	2690 ⁺²⁰⁰ ₋₁₇₀ K	2560 ± 120 K	2320 ⁺⁵⁰ ₋₆₀ K	350 ± 70	232 ± 20	2.5	2.9	166 ⁺²² ₋₁₉	4.9
0.118	2460 ± 160 K								
0.130	2450 ⁺¹⁶⁰ ₋₁₅₀ K	2470 ± 100 K	2400 ⁺⁵⁰ ₋₆₀ K	291 ± 50	274 ⁺¹⁹ ₋₂₄	1.9	2.0	224 ⁺²⁵ ₋₂₆	4.7
0.142	2840 ⁺²⁶⁰ ₋₂₂₀ K								
0.153	2220 ⁺¹⁵⁰ ₋₁₄₀ K								
0.165	2210 ± 150 K	2320 ± 100 K	2390 ⁺⁴⁰ ₋₅₀ K	230 ± 50	255 ± 26	1.4	1.5	250 ⁺¹⁵ ₋₁₆	3.8
0.177	2430 ± 160 K								
0.212	2050 ⁺¹⁵⁰ ₋₁₆₀ K	1940 ⁺¹²⁰ ₋₁₁₀ K	1980 ⁺⁷⁰ ₋₈₀ K	100 ⁺³⁰ ₋₄₀	118 ± 17	0.7	0.9	114 ± 16	2.9
0.224	1780 ⁺¹⁸⁰ ₋₂₇₀ K								

Table 4. The common-mode derived blackbody temperatures of HAT-P-2b in the HST WFC3 G141 bandpass for the planetary orbital phases during the second HST visit. These temperatures are also plotted in Figure 6. In the third through tenth columns we group the phases together like in Figure 10. The third column denotes retrieved temperatures without priors. For the fourth column we included a prior on the spectral monochromatic offset from the white light-curve. The fifth, sixth and ninth columns show the monochromatic offset to be applied to the common-mode retrieved spectra. Because they describe the variations in the detected white-light, which includes telescope systematics, these offsets should be compared between methods rather than between phases. In the seventh, eighth and tenth column we denote the reduced chi-squared values of the fits. The blackbody fits perform markedly better, but as noted in the text, they are still unreliable.

between the third energy level and the fifth. It is the most prominent stellar line at G141 wavelengths.

To investigate the origin of this apparent excess flux, we first performed the common-mode method at the WFC3 native resolution, and found a flux excess in all five pixel-sized wavelength bins around 1.28 μm . We therefore collected these five wavelength columns into a single bin. To compare this bin to the rest of the spectrum, we created two extra wavelength bins that surround the 1.28 μm bin and that are unaffected by the stellar Pa β line. The three bins are shown in the right panels of Figure 12.

Similarly to Section 5.1 we fitted a blackbody through the common-mode spectra at the native WFC3 resolution, this time excluding the three wavelength bins discussed above. We subtracted the flux expected by the blackbody fit from the common-mode reduced spectra and we plot the deviation from this blackbody, δ_{Pa} , in the lower panel of Figure 12. Recall that, in order to find the common-mode reduced spectrum of an orbit, its spectrum has to be divided by the in-eclipse spectrum. Therefore, if the in-eclipse spectrum is

anomalous by one standard deviation due to statistical scatter, all common-mode reduced spectra will appear anomalous in the opposite direction by the same value. However, the mean of the Paschen line bin deviates from the blackbody model by 4.1 σ , while the other two bins deviate by only 0.3 σ . The mean difference between the Paschen line bin and the other bins in the second visit is three times its measurement uncertainty. That difference is smaller in the first visit, but still at 1.8 σ . The flux excess for the first visit may therefore possibly originate from strong noise in the in-eclipse spectrum. However, this still leaves the extra excess in the second visit unexplained. Also, the match with the atomic Pa β line is unlikely to be coincidence.

The Paschen line bin does not contain any strong flat-field artefacts and there are no bright background stars. There also appear to be no abnormal detector defects, and there is no anomaly in the number of detected cosmic rays around 1.28 μm .

A drift of the spectrum on the detector in the wavelength direction in combination with the undersampling of the stel-

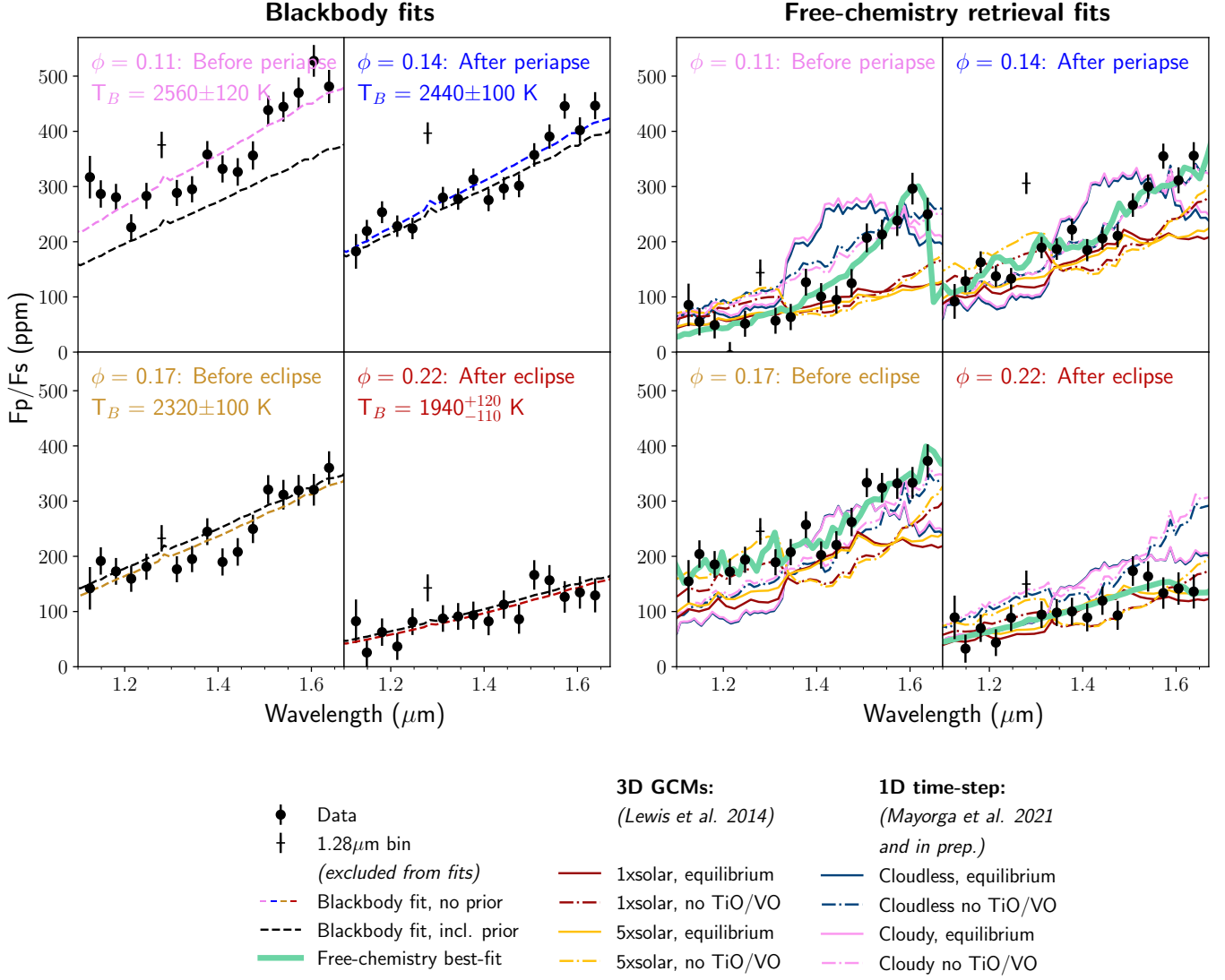


Figure 10. Partial phase curve spectra for HAT-P-2b of the second visit for the common-mode method (black data) compared to forward models and the 1D free-chemistry retrieval (aquamarine green). The 3D GCMs are represented in red for the solar metallicity scenario and in yellow for the 5 \times solar metallicity scenario. 1D cloudless solar metallicity forward models by (Mayorga et al. 2021, and in prep.) are depicted in blue, while cloudy models are shown in pink. Equilibrium cases are denoted with solid lines, and cases excluding TiO and VO are represented with dash-dotted lines. Dashed lines represent fits of a blackbody spectrum plus a monochromatic offset. The fits without priors are colored and the fits including temperature priors from the white light-curve, are black. Any features in the blackbody fits are of stellar origin. We excluded the wavelength bin at 1.28 μm from the fits. In the four panels on the left, the common-mode spectra have been shifted with a monochromatic offset that fits the blackbody spectra without priors. In the four panels on the right they are shifted to best fit the 1D free-chemistry retrievals. Due to the nature of the common-mode method, these offsets are not known *a priori*. The big difference in monochromatic offset between the blackbody fits and the free-chemistry retrievals is readily visible and quantified in Table 4.

lar Pa β line can deteriorate the quality of WFC3 spectra (Deming et al. 2013). However, on an orbit-to-orbit basis there was very little drift in the wavelength direction during the second visit (see Figure 2b). Also, we negated this effect by centering any wavelength bin around the Pa β line. This way, if the core of the line shifts slightly from one pixel to another, the line as a whole stays in the same bin and the total flux in that bin is therefore stable.

Whereas there is almost no drift in the wavelength direction during the second visit, we observe a visit-long drift of 0.8 pixels in the spatial-scan direction. The IR WFC3 flat-field is uncertain at a 1% level. Given a scan-length of 400 pixels, we estimate that this drift may introduce a maximum uncertainty of $2 \times 0.01 \times 0.8/400 = 40$ ppm per wavelength channel at the WFC3 native resolution. This is insufficient and it tends to average out over multiple pixels.

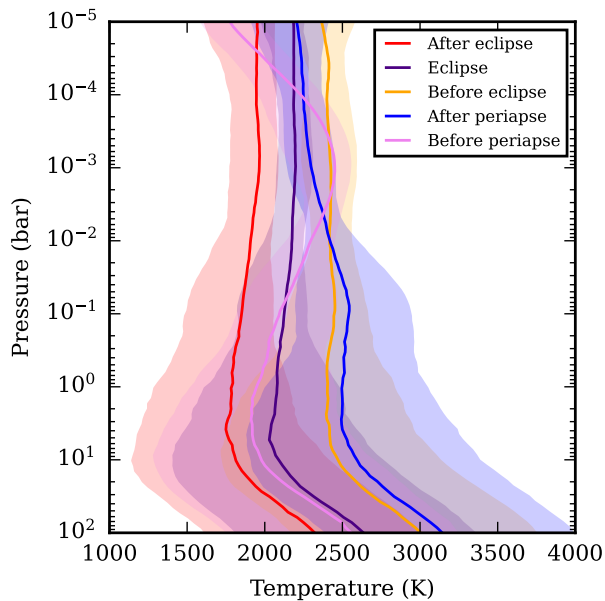


Figure 11. Median retrieved temperature-pressure profiles for the partial phase curve spectra. The shaded regions denote the 1σ uncertainties. The solid lines are median TP-profiles. The spectra are shown in Figure 10.

Curiously, the maximum deviation in Figure 12 occurs after periastron, but before the white light maximum of the planet. This suggests that there is a possible connection to the planet’s orbit and that the response is quicker than the planetary atmospheric layers probed by the WFC3 continuum. We further discuss astrophysical origins for this flux excess in Section 6.4.

5.4. Stellar contamination

A prerequisite for the correct application of the common-mode method is the absence of variations in the stellar spectrum. In this subsection we estimate the effects that a change in effective stellar temperature may have on the common-mode spectra. To do so, we used `pysynphot` (STScI Development Team 2013) and generated a Kurucz stellar spectrum (Kurucz 1993) with stellar parameters closest to those observed for HAT-P-2 (Tsantaki et al. 2014). We adopted this stellar spectrum as the in-eclipse spectrum. Subsequently, we generated another Kurucz spectrum, but with an effective temperature that is 0.5 K lower and we assumed this to be an out-of-eclipse spectrum. For the sake of this argument, we set any planetary contribution to zero. Following the common-mode method stipulated by Arcangeli et al. (2021), we divided the mock out-of-eclipse spectrum by the mock in-eclipse spectrum and retrieved the spectrum shown in blue in Figure 13. This surprisingly mimics the planetary spectra seen in Figure 10. Pretending that the spectrum in Figure 13 was produced by a planet, we fitted a planetary blackbody

to it plus a monochromatic offset and we retrieved a blackbody temperature of 1830 K, displayed as a dashed, golden line. The mean difference between the two stellar spectra is approximately of the size of the constructively interfering stellar pulsations in white light. However, if stellar pulsations would truly change the effective stellar temperature in the way presented above, the star-induced slope in Figure 13 would become negative, pushing for “negative” temperatures in Figure 6. This leaves open the possibility that the stellar effective temperature changed on a longer timescale throughout the second visit.

Also notable, is that a change in stellar temperature can induce a deviation from a planetary blackbody model like the deviation, δ_{Pa} discussed in Section 5.3. However, for a difference in stellar effective temperature of 0.5 K, this effect is on the order of just 10 ppm, far smaller than the deviation observed in Figure 12. If the pulsations were the cause of the excess flux discussed in Section 5.3, the excess flux should correlate with the pulsations in the lower left panel of Figure 12. We only observe a Pearson correlation coefficient with δ_{Pa} of -0.46 at a p-value of 0.06. There is also no significant $Pa\beta$ flux excess when comparing groups of exposures taken during a pulsation peak to groups of exposures taken during a pulsation trough.

Also, this effect is quantitatively not a satisfactory explanation for the flux excess discussed in Section 5.3, unless the stellar effective temperature changed by ~ 15 K throughout the visit and the telescope systematics counteracted this accordingly. However, such a large temperature change and hence large white-light variations would have been noticed before at other wavelengths (Bakos et al. 2007; Lewis et al. 2013; de Wit et al. 2017).

The effect discussed in this section only affects common-mode reduced planetary spectra. In light-curve fitting methods, the stellar contamination would be filtered out with the visit-long polynomials or stellar pulsations.

6. DISCUSSION

The shape and timing of maximum and minimum planetary flux from the phase curve offer significant insights into HAT-P-2b’s atmospheric properties, reflecting thermal variations resulting from time-variable heating. Comparing phase variations at different wavelengths provides further understanding of the atmosphere’s thermal, wind, and chemical structure.

6.1. Light-curve comparison to the forward models

While the general shape and timing of the white light-curve is similar to that of the forward models, both underestimate the peak flux. The product of hydrogen dissociation, H^- , exhibits significant opacities at near-infrared wavelengths (Arcangeli et al. 2018), consequently reducing the

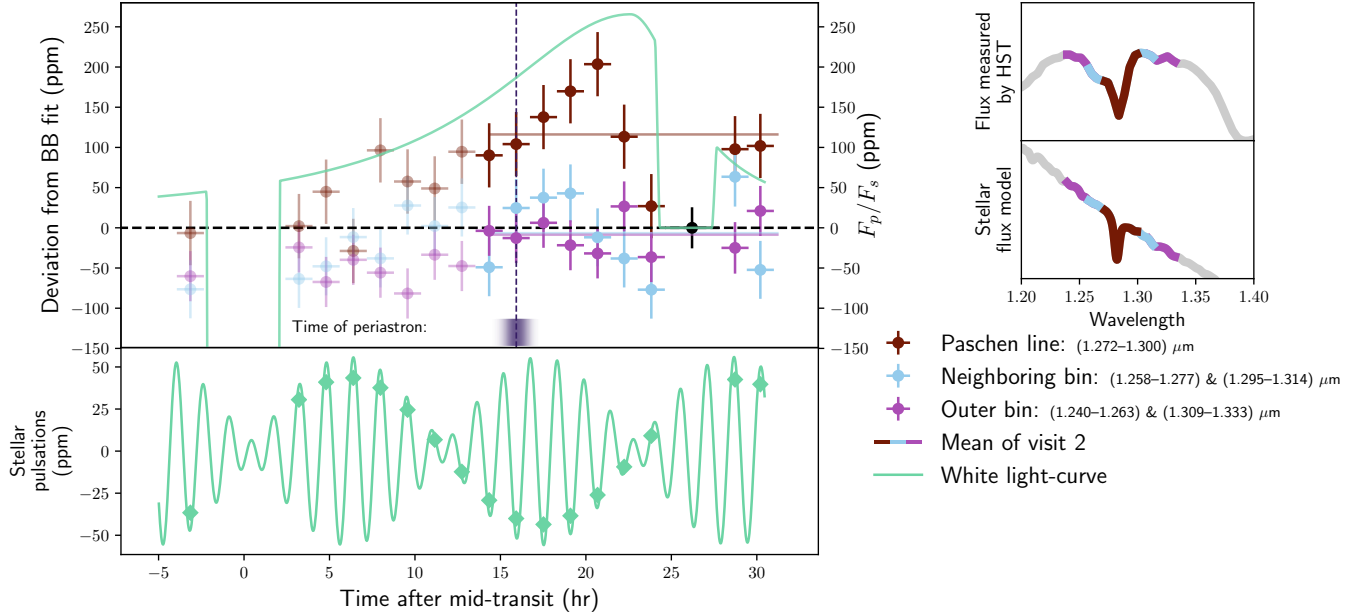


Figure 12. Excess flux of the common-mode reduced spectra at $1.28 \mu\text{m}$.

Left: Deviation from a planetary blackbody model for three wavelength bins surrounding the stellar $\text{Pa}\beta$ line. For the dark red bin this equals δ_{Pa} . This planetary blackbody model was fit to the common-mode reduced spectra excluding the wavelength bins shown in this figure for each orbit at WFC3’s native resolution. The black point in eclipse denotes the uncertainty on the in-eclipse flux measurement. In the common-mode method all data is divided by this in-eclipse data. Therefore, this uncertainty also represents the uncertainty on the mean deviation of each bin. We denote the mean deviation in the second visit with a horizontal line. The data for the first visit is faded because Section 2.5 determined that the common-mode method is unreliable for the first visit. We plot the median planetary light-curve from Figure 2 in aquamarine green in the background for reference of the timing of the peak in the excess flux. Its scale (right axis) is the same as for the binned data. The lower panel contains the corresponding stellar pulsation with the pulsation amplitude averaged over each orbit denoted as diamonds. Also denoted is the posterior distribution of the time of periastron from this work. The posterior median is demarcated with a vertical dashed line.

Right: Wavelength binning used for the $\text{Pa}\beta$ line analysis in the left panel. The upper panel shows an example measured spectrum of a single WFC3 exposure. The dip in flux at $1.26 \mu\text{m}$ is due to a dip in the G141 transmission function. The lower panel shows a PHOENIX stellar spectrum for HAT-P-2 (Husser et al. 2013) smoothed to the WFC3 G141 dispersion resolution. The $\text{Pa}\beta$ line at $1.282 \mu\text{m}$ is clearly discernible and has a band-averaged depth of $\sim 5\%$. We collected the five WFC3 pixel-wide columns surrounding the $\text{Pa}\beta$ line into the dark red bin. The 6 neighboring pixel-wide columns were binned into the light blue bin and the 8 columns surrounding that were grouped into the outer, magenta bin. None of the bins contain any wavelengths of the other bins.

pressures probed by WFC3. In the case of an inverted TP-profile, this would also increase the probed temperature at the peak of the light-curve. An overabundance of H^- compared to the chemical equilibrium models may therefore explain the underestimated peak flux. Furthermore, the strong contrast between the flux increase timescale of $c_3 = 9.1_{-2.1}^{+3.4}$ hr to the flux decrease timescale of $c_4 = 3.9_{-0.6}^{+0.7}$ hr also indicates an enhanced H^- abundance: as the planet heats up, H^- is formed near-instantaneously in the hotspot (Bell & Cowan 2018; Arcangeli et al. 2021), prompting the formation of a thermal inversion, and decreasing the pressures probed by WFC3. Those layers have a shorter radiative timescale than the layers probed during the heating phase. This notion is corroborated by Figure 9: the best-fit 1D-retrieval probes higher altitude layers at shorter wavelengths than the forward models predict. Enhanced H^- abundances are consistent with the 1D free-chemistry retrievals. This extra H^- abundance with respect to the thermal equilibrium of models may orig-

inate from disequilibrium processes like photochemistry, as has been suggested for a couple other planets (Lewis et al. 2020; Jacobs et al. 2022). However, an increased H^- opacity and therefore the probing of lower pressure layers, does not explain the big divergence between flux decrease timescale at $4.5 \mu\text{m}$ (10.3 ± 1.5 hr; de Wit et al. 2017) and at WFC3 wavelengths (Parmentier et al. 2018).

Alternatively, horizontal advection, and therefore wind speeds, may be higher than in the WFC3 photosphere than at the lower pressures probed by Spitzer, which is theoretically qualitatively in line with the GCM results by Lewis et al. (2014), albeit not quantitatively. Stronger mixing decreases the radiative timescale for the planet as a whole because it is inversely proportional to the temperature cubed (Iro et al. 2005; Seager et al. 2005).

We measure a lag in the planetary peak brightness with respect to the incident stellar flux. This is partially due to the finiteness of the atmospheric radiative timescale (Iro & Dem-

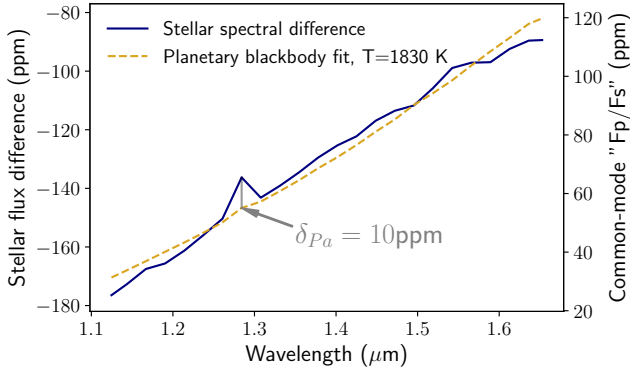


Figure 13. Spectral difference between two Kurucz stellar spectra of HAT-P-2 with a 0.5 K difference in effective temperature. Suppose that the hotter stellar spectrum is the observed in-eclipse spectrum and that the cooler spectrum is the out-of-eclipse spectrum. If we perform a common-mode method on this, the resultant F_p/F_s is shown on the right axis with the best-fit blackbody being a dashed line. Also, note that in this case the Paschen β deviation (see Section 6.4) is measured to be 10 ppm. All wavelength bins contain 5 wavelength pixel-columns. The δ_{Pa} in this figure therefore corresponds to the dark red bin in Figure 12.

ing 2010; Cowan & Agol 2011), and partially the result of the viewing geometry with more and more of the hotter dayside coming into view after periapse. This work’s measurement of the peak flux delay of $c_2 = 6.7 \pm 0.6$ hr is only slightly longer than the 1D time-stepping models (3-5 hours after periastron), the 3D GCMs (peak 4-5 hours after periastron), as well as the $4.5 \mu\text{m}$ Spitzer peak flux delay (5.40 ± 0.57 hr).

The imperfect fit between the forward models and the fitted light-curve may also be the result of planetary variability. Lewis et al. (2014) measured the eclipse depth variability of HAT-P-2b in their GCMs without a thermal inversion. The planet’s eclipse depth is likely variable by a maximum of $\sim 20\%$ at G141 wavelengths.

6.2. Interpretation of spectral retrievals

The 1D free-chemistry retrievals strongly depend on the monochromatic offset. We tried to mitigate this by assuming a prior on this offset leveraged from the white light-curve fits. However, the common-mode method was devised by Arcangeli et al. (2021) to monitor partial phase-curves in a non-continuous way, inhibiting the use of light-curve fits. Without prior on the offset, the free-chemistry retrievals show an even wider array of possible atmospheric compositions. Additionally, the free-retrievals find significantly different adiabats below the radiative-convective boundary (Figure 11). The rapid changes in irradiation that HAT-P-2b experiences are not expected to alter these deep layers in such a short time frame. The retrievals would be more robust if thermo-chemical equilibrium retrievals, which require fewer fit parameters, were used for common-mode reduced spectra (see

e.g. Arcangeli et al. 2018; Coulombe et al. 2023). However, those models are *a priori* in an instantaneous equilibrium, while eccentric planets are not. As such, equilibrium models are less sensitive to the thermo-chemical processes taking place during the heating/cooling of the planet, and they may present less accurate results.

Changeat et al. (2022) retrieved a secondary eclipse spectrum from the same WFC3 data as we analyzed in this work (for a detailed comparison in methodology, see Appendix A). Their spectrum is most consistent with a blackbody spectrum, although their 1D free-chemistry retrieval found some tentative evidence ($\mathcal{B} < 1$) for a non-inverted TP-profile with H_2O and VO in absorption. Those results are consistent with the findings of this work within the margins of uncertainty.

6.3. An isothermal atmosphere?

One of the key questions surrounding HAT-P-2b discussed in previous works was the possible presence of a (transient) thermal inversion in HAT-P-2b’s atmosphere (Lewis et al. 2013; Mayorga et al. 2021). We tested this using 1D free-chemical retrievals in Sections 4.5 and 5.2. We found a thermal inversion that disappears after periapse. The transient thermal inversions predicted by the 1D and 3D forward models indeed commence before periapse, but they also persist well into secondary eclipse.

The tentative thermal inversion before periapse is driven by the 2.3σ detection of H^- bound-free absorption. However, H^- could not be significantly detected in any subsequent spectra. Also, its retrieved volume mixing ratio of $-4.2^{+0.4}_{-0.5}$ is 3-4 orders of magnitude higher than thermo-chemical equilibrium models predict for KELT-9b (Jacobs et al. 2022) and WASP-18b (Coulombe et al. 2023), both of which are hotter than HAT-P-2b. The retrievals also find the H^- at much higher altitudes, where it should have an even lower abundance due to the mutual neutralization with positive ions (Lothringer et al. 2018).

Alternative fits to the before-periapse spectrum and the spectral retrievals at later phases, result in unrealistically high abundances of TiO at low significances. The WFC3 secondary eclipse spectrum is excellently fit with a blackbody. HAT-P-2b’s near-infrared spectrum is therefore most likely near-featureless from periastron to eclipse. This would mean that there is an extra slope in the phase-resolved spectra that the common-mode method could not account for and that leads to a spurious almost-detection of H^- before periapse. A possible source of the extra slope is small variations in the stellar effective temperature (Section 5.4). While the slopes of the common-mode-retrieved spectra may be unreliable, this is not necessarily true for spectral features obtained through this method.

The retrievals are one dimensional, while the planet is intrinsically three-dimensional. The equilibrium GCMs pre-

dict a local thermal inversion in just the planet’s hotspot and a non-inverted TP-profile in the surrounding region on the dayside. The combined modeled spectrum shows a thermal inversion. However, the retrieved median TP-profiles after periape are nearly isothermal. The individual solutions for each spectrum are less isothermal, but averaged over all solutions combine into near-isothermals. This shows that there are multiple possible solutions to each spectrum and that the actual emission spectra may be a combination of several distinct spectra emerging from chemically distinct areas of the dayside. Applying 1-dimensional retrievals to an intrinsically 2D/3D planet can lead to biased results and spurious detections of elements (Taylor et al. 2020). However, a full 3D thermo-chemical equilibrium retrieval (Challener & Rauscher 2022) is outside the scope of this paper and the data precision does not warrant such a complex model.

By the time of secondary eclipse, the Earth-facing hemisphere-averaged thermal structure of the atmosphere has not been fully inverted yet as predicted by the forward models. This is at odds with the predictions of forward models. The chemistry in the forward models responds to the changing temperature instantaneously, while in reality it might take time. However, as shown by Parmentier et al. (2018); Arcangeli et al. (2021), the dissociation/recombination timescales of H_2 and TiO , the prime agent for thermal inversions, are on the order of seconds. Therefore, there must be other processes at play, like advection, that prevent the swift emergence of a strong thermal inversion. Additionally, the onset of rapid dissociation would help transition the hotspot of the planet from a low-ionization to a high-ionization state. This may result in the coupling of the gas flow in the hotspot to the local magnetic field. This could induce excess heating (Helling et al. 2021), and control large-scale dynamics in and around the ionized region (Rogers & Komacek 2014; Beltz et al. 2022). This could therefore also impact the timescale over which thermal inversions could develop.

It is unlikely that the blackbody-like spectra are produced by lofty clouds as clouds can considerably cool down a planet, which is not observed here. The sedimentation efficiency chosen for the cloudy forward models ($f_{sed} = 0.5$) is already low for a high-gravity planet like HAT-P-2 (Saumon & Marley 2008; Gao et al. 2018).

6.4. Paschen β line

In Section 5.3 we observed a flux excess in a wavelength bin that coincides with the Paschen β line, the most prominent stellar line at G141 wavelengths. It is persistent throughout HAT-P-2b’s phase curve and it peaks between periastron and the peak of the white light-curve. This feature was found with the common-mode method, but it is also visible in the RECTE-reduced eclipse spectrum as well as in the eclipse spectrum derived by Changeat et al. (2022). We assessed that

this spectral feature is unlikely to be noise, unlikely to be the result of a change in stellar effective temperature, and it is unlikely to be of telescopic origin. In this section we briefly discuss other possible astrophysical origins.

As HAT-P-2b approaches its host star, its upper atmosphere is shock heated. Due to the short radiative timescales, the upper atmosphere experiences the most rapid changes and its temperature will peak before the lower atmosphere’s temperature peaks (Lewis et al. 2014). Atomic/molecular lines probing upper layers therefore peak earlier than lines probing deeper layers.

Studies on hotter exoplanets found that non-local thermal equilibrium (NLTE) effects in the upper atmosphere can significantly heat up the planetary upper atmosphere as well as alter the populations of hydrogen electron energy levels (Wyttenbach et al. 2020). NLTE effects therefore increase the strength of some planetary hydrogen lines in the transmission spectrum (Fossati et al. 2021; Borsa et al. 2021), which may include $Pa\beta$. However, NLTE effects on specific hydrogen lines have only been found in high-resolution spectra as they probe higher atmospheric layers than emission spectroscopy.

Sánchez-López et al. (2022) found planetary $Pa\beta$ absorption in KELT-9b’s transit. They interpret their detection as hydrogen absorption from atmospheric layers at $\sim 1.3 R_p$. As an alternative, they entertain the thought that the absorption may originate from hydrogen atoms escaping the planet after stellar activity. This presents an analogy to HAT-P-2b’s shock heating during periape.

Alternatively, the signal in the $1.28 \mu m$ bin could be induced by the planet on the host star. Star-planet interactions can have many forms and they have been observed on multiple planets (Shkolnik et al. 2008; Désert et al. 2011; Vitto 2020; Bryan et al. 2024), including the pulsations on HAT-P-2 (de Wit et al. 2017). We did not observe a significant stellar dimming corresponding to $>2 K$. Hence, if the $Pa\beta$ signal is indeed induced by the planet, the planet’s effect on that line must be greater than on the stellar continuum. The stellar Paschen line originates from higher altitudes in the stellar atmosphere than the continuum. It is therefore not inconceivable that only these higher layers temporarily either heat up or expand due to either external effects or the stellar pulsations, although δ_{Pa} is only weakly correlated with the pulsations.

The interplay between the planetary magnetic field and the stellar magnetic field is found to induce chromospheric activity in planetary host stars (Cauley et al. 2019). Cuntz et al. (2000) propose that orbiting planets induce magnetic reconnecting events between the planetary and stellar magnetospheres which could lead to magnetic heating. Chromospheric activity is typically monitored through variations in the Ca II H&K line strength, but the $Pa\beta$ line is sometimes also used as an activity indicator (Schmidt et al. 2012;

Fuhrmeister et al. 2023). Being a massive planet, HAT-P-2b likely has a strong magnetic field (Yadav & Thorngrén 2017; Arcangeli et al. 2019). Magnetic field line interactions are inversely proportional to the squared distance between the star and planet (Cuntz et al. 2000), which means that chromospheric activity should be strongly biased to the time the HAT-P-2b is closest to its host star. Klein et al. (2021) found correlations between the rotation of the magnetic pole of AU Mic with the strength of the stellar Pa β line.

However, this does not very well explain that the 1.28 μm bin has a clear minimum during eclipse. Also, whereas the flares on AU Mic could originate from star-planet interactions (Ilin & Poppenhaeger 2022), no multi-wavelength flare events have yet been discovered for HAT-P-2 (Ilin et al. 2024).

Alternatively, the stellar heating may be caused by the Poynting flux communicating magnetic field energy from the planet to the star for sub-Alfvénic interaction, which is analogical to Io’s or Ganymede’s auroral footprint on Jupiter (Saur et al. 2013; Hue et al. 2023; Sulaiman et al. 2023). If the planet’s Alfvén Mach number becomes larger than one (which occurs at 0.08 AU around the Sun), the magnetic interaction drops steeply, which may be the case at HAT-P-2b’s apastron (0.1 AU). However, Figueira et al. (2016) were unable to find any correlations between the planetary distance and stellar activity indicators for the even more eccentric HD 80606b, which also orbits a quiescent star.

7. SUMMARY

In this work, we investigated the atmospheric dynamics and chemistry of the highly-eccentric close-in giant HAT-P-2b by spectroscopically measuring its partial phase curve using WFC3. We fitted the white light-curve using an asymmetric Lorentzian and found the peak flux to occur $c_2 = 6.7 \pm 0.6$ hr after periastron, $\sim 2\sigma$ longer than forward model predictions and previous observations. We find a relatively large difference between the flux increase ($c_3 = 9.1^{+3.4}_{-2.1}$ hr) and decrease ($c_4 = 3.9^{+0.7}_{-0.6}$ hr) timescales. We explain this as well as the delayed peak flux with the possible emergence of H⁻ opacities during periastron passage as higher altitudes are probed with shorter radiative timescales. Furthermore, we found that the observed geometry of the system has evolved since the Spitzer observations almost a decade earlier, but that the orbital harmonics stellar pulsations have likely remained remarkably stable. Mid-transit time took place at $t_0 = 2459204.11219 \pm 0.00014$ BJD TDB, which is discrepant with previous measurements (Ivshina & Winn 2022) at 3.3σ , and the argument of periastron changed from $\omega_\star = 188.44 \pm 0.43$ degrees in 2011 to $\omega_\star = 191.6^{+1.9}_{-2.0}$ degrees in December 2020. We measure the time of periastron to take place 15.9 ± 0.5 hr after mid-transit, which is 0.67 ± 0.5 hr later than in the epoch observed by de Wit et al. (2017) but

consistent with the predictions from de Beurs et al. (2023) for the current observation epoch (December 2020).

We searched for the planet-induced stellar pulsations found by de Wit et al. (2017) by fitting for two stellar pulsation modes at 79 and 91 times the orbital frequency of the planet. Indeed, we retrieve these pulsations at high significance ($\Delta\text{BIC}=21$) and at amplitudes similar to those found at 4.5 μm . Because of their small, seemingly monochromatic amplitudes, they should have little effect on the planetary climate and spectral continuum.

The measured transmission spectrum is flat as expected because of the computed small scale height for this planet, allowing us to provide a refined measurement of the planet’s radius: $R_p^2/R_s^2 = 0.004869 \pm 0.000012$. The secondary eclipse spectrum is very well fit by a blackbody spectrum, and is therefore consistent with a mostly isothermal TP-profile. No molecules could be detected with high significance ($>3\sigma$).

We applied the common-mode method by Arcangeli et al. (2021) to a partial WFC3 phase curve of HAT-P-2b with mixed results. The first visit was visibly too affected by telescope systematics. The second visit was less affected by instrumental effects, but the resulting spectra have a different spectral slope than expected. We show that small changes in stellar effective temperature can have outsized effects on the spectral slope measured by the common-mode method. Both the blackbody fits as well as the free-retrievals that used priors from the white light-curve fits, show inadequate results stemming from the monochromatic offset introduced by the common-mode method. This translates into blackbody fits with higher temperatures than expected and deep atmosphere adiabats that change unphysically through time. Future partial phase curves with HST will face the same issues.

However, the common-mode reduced spectra of the partial phase curve revealed an anomalously high flux in the spectroscopic bin that coincides with the hydrogen Paschen β line and is irrespective of spectral slope or monochromatic offset. On average, it deviates by 4.1σ from a planetary blackbody model over the duration of the second visit. The flux excess is unlikely to be of instrumental origin and it is not affected by the above mentioned challenges for common-mode reduced spectra. It is therefore likely of astrophysical origin. It does not seem to be correlated to stellar pulsations, but a stellar origin is not excluded. Ground-based emission spectroscopy focusing on additional hydrogen lines and potentially the helium line at 1.0833 μm could elucidate the source of the flux excess in the Pa β bin.

We thank L. Kreidberg for their contribution to the proposal that led to this paper, and we thank V. Panwar and H. Shivkumar for the interesting discussions. J.M.D acknowledges support from the Amsterdam Academic Alliance

(AAA) Program, and the European Research Council (ERC) European Union’s Horizon 2020 research and innovation program (grant agreement no. 679633; Exo-Atmos). This work is part of the research program VIDI New Frontiers in Exoplanetary Climatology with project number 614.001.601, which is (partly) financed by the Dutch Research Council (NWO). Support for program HST-GO-15131 was provided by NASA through a grant from the Space Telescope Science Institute, which is operated by the Associations of Universities for Research in Astronomy, Incorporated, under NASA contract NAS5-26555. Z.L.D. would like to thank the generous support of the MIT Presidential Fellowship, the MIT Collamore-Rogers Fellowship and to acknowledge that this material is based upon work supported by the National Science Foundation Graduate Research Fellowship under Grant No. 1745302. Z.L.D. acknowledges support from the D.17 Extreme Precision Radial Velocity Foundation Science program under NASA grant 80NSSC22K0848.

Facilities: HST (WFC3), Spitzer (IRAC)

Software: `astropy` (Astropy Collaboration et al. 2013), `batman`, (Kreidberg 2015b) `emcee`, (Foreman-Mackey et al. 2013) `exoCTK` (Bourque et al. 2021), `lmfit` (Newville et al. 2014), `matplotlib` (Hunter 2007), `pandas` (pandas development team 2020), `POSEIDON` (MacDonald & Madhusudhan 2017; MacDonald 2023), `PyMSG` (Townsend & Lopez 2023), `PyMultiNest` (Feroz et al. 2009; Buchner et al. 2014), `pysynphot` (STScI Development Team 2013), `Python` (Van Rossum & Drake Jr 1995), `scipy` (Virtanen et al. 2020), `seaborn` (Waskom 2021), `RECTE` (Zhou et al. 2017),

APPENDIX

A. SPECTRUM COMPARISON TO PREVIOUS STUDIES

Changeat et al. (2022) and Edwards et al. (2023) recently observed HAT-P-2b’s secondary eclipse spectrum and transmission spectrum respectively. They used the same data presented in this work, but they used Iraclis (Tsiaras et al. 2016) to reduce the data and they used an exponential-ramp method (e.g. Kreidberg et al. 2014) to fit for the telescope systematics in the white light-curve. To find the transmission and eclipse spectra, they used the same orbits as we used in this work, but they removed the first exposure of each orbit. They divided each spectroscopic light-curve by the telescope systematics model derived from the white light-curve (divide-white method; Kreidberg et al. 2014) and then fit a secondary eclipse/transit model to the detrended light-curve.

We compare the spectra from Changeat et al. (2022) and Edwards et al. (2023) to the spectra from this work in Figure 14. Their uncertainties on each data point are 40% and 80% larger than the uncertainties presented in this work for the eclipse and transit spectra respectively. This difference is partially explained by them splitting the light into 50% more wavelength bins and discarding every first exposure of every orbit. Also, they conducted separate fits for the eclipse and transit events, whereas our approach involves simultaneous fitting, informing the fits of one event with the orbit-long ramp shape from the other.

Changeat et al. (2022) fit for a planetary emission model constant with time, while we used an asymmetric Lorentzian phase curve model, which has a decreasing planetary flux around eclipse. If we had followed their emission model, the retrieved eclipse spectrum would have been $\sim 45 \text{ ppm } \mu\text{m}^{-1}$ steeper. This is largely mitigated by the difference in light-curve fitting methods: while the “divide-white” light-curve fitting method corrects wavelength-independent flux changes effectively (see e.g. Kreidberg et al. 2014; Barat et al. 2024), it tends to underfit wavelength-dependent systematics, notably HST’s orbit-long ramps. This wavelength dependence of the orbit-long ramps is especially evident when the product of the stellar spectrum with the G141 transmission function is strongly wavelength-dependent (Kreidberg et al. 2014; Jacobs et al. 2022). This is the case for HAT-P-2, introducing an extra negative slope of $\sim -20 \text{ ppm } \mu\text{m}^{-1}$ into the spectrum of Changeat et al. (2022). The remaining $\sim -25 \text{ ppm } \mu\text{m}^{-1}$ is unexplained for, but well within the measurement uncertainties of $60 \text{ ppm } \mu\text{m}^{-1}$.

Another notable difference is that the eclipse depth of the bin centered at $1.28 \mu\text{m}$ is much deeper for Changeat et al. (2022). This is mainly caused by the choice of binning: Changeat et al. (2022) chose narrower bins, such that their $1.28 \mu\text{m}$ bin solely includes light from the Pa β line. This is in contrast to the bin from this work, which also contains two pixel-wide columns at wavelengths shorter than $1.277 \mu\text{m}$. Those two columns do not show the Paschen anomaly discussed in Section 5.3. Another reason why the $1.28 \mu\text{m}$ bin is more anomalous in the Changeat et al. (2022) spectrum, is that the Pa β bin shows a stronger

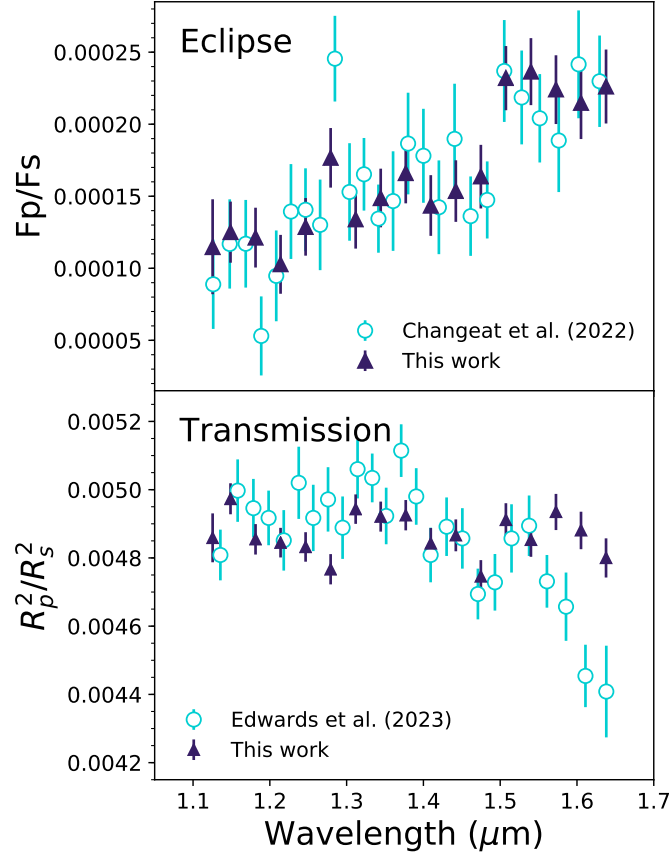


Figure 14. Comparison of the secondary eclipse and transmission spectra from previous studies to the ones presented in this study. Purple spectra denote spectra from this work and cyan spectra are from [Changeat et al. \(2022\)](#) and [Edwards et al. \(2023\)](#).

planetary flux decrease around eclipse than the surrounding bins (see Figure 12). The difference in eclipse depth because of the assumed planetary light-curve is therefore greater than in the surrounding bins.

The transit depths found by [Edwards et al. \(2023\)](#) decrease with wavelengths, whereas the spectrum found by this work is flat. We found that we could reproduce the downward slope observed by [Edwards et al. \(2023\)](#) by using the same ramp amplitude parameter for all orbits. A single shared ramp amplitude is not common-practice (see e.g. [Kreidberg et al. 2014](#)) as the first non-discarded orbit is often fit with a different ramp amplitude than the rest. The WFC3 ramp amplitudes depend on the incoming flux and therefore also on wavelength ([Zhou et al. 2017](#)). As shown in Figure 1 of [Jacobs et al. \(2022\)](#), the difference in ramp amplitude between the first non-discarded WFC3 orbit and the other orbits is therefore wavelength dependent. By inadequately fitting the ramp amplitude of the single orbit before transit, [Edwards et al. \(2023\)](#) therefore introduced a spurious slope to the transmission spectrum. [Changeat et al. \(2022\)](#) used the same exponential-ramp model as [Edwards et al. \(2023\)](#) to fit their secondary eclipse data. However, their emission spectrum is not biased by the single-ramp-amplitude assumption because the secondary eclipse measurements were preceded by more than a dozen orbits with the same ramp amplitude.

B. ADDITIONAL TABLES AND FIGURES

REFERENCES

- Ackerman, A. S., & Marley, M. S. 2001, *ApJ*, 556, 872,
doi: [10.1086/321540](https://doi.org/10.1086/321540)
- Adcroft, A., Campin, J.-M., Hill, C., & Marshall, J. 2004, *Monthly Weather Review*, 132, 2845, doi: [10.1175/MWR2823.1](https://doi.org/10.1175/MWR2823.1)
- Arcangeli, J., Désert, J. M., Parmentier, V., Tsai, S. M., & Stevenson, K. B. 2021, *A&A*, 646, A94,
doi: [10.1051/0004-6361/202038865](https://doi.org/10.1051/0004-6361/202038865)
- Arcangeli, J., Désert, J.-M., Line, M. R., et al. 2018, *ApJL*, 855, L30, doi: [10.3847/2041-8213/aab272](https://doi.org/10.3847/2041-8213/aab272)

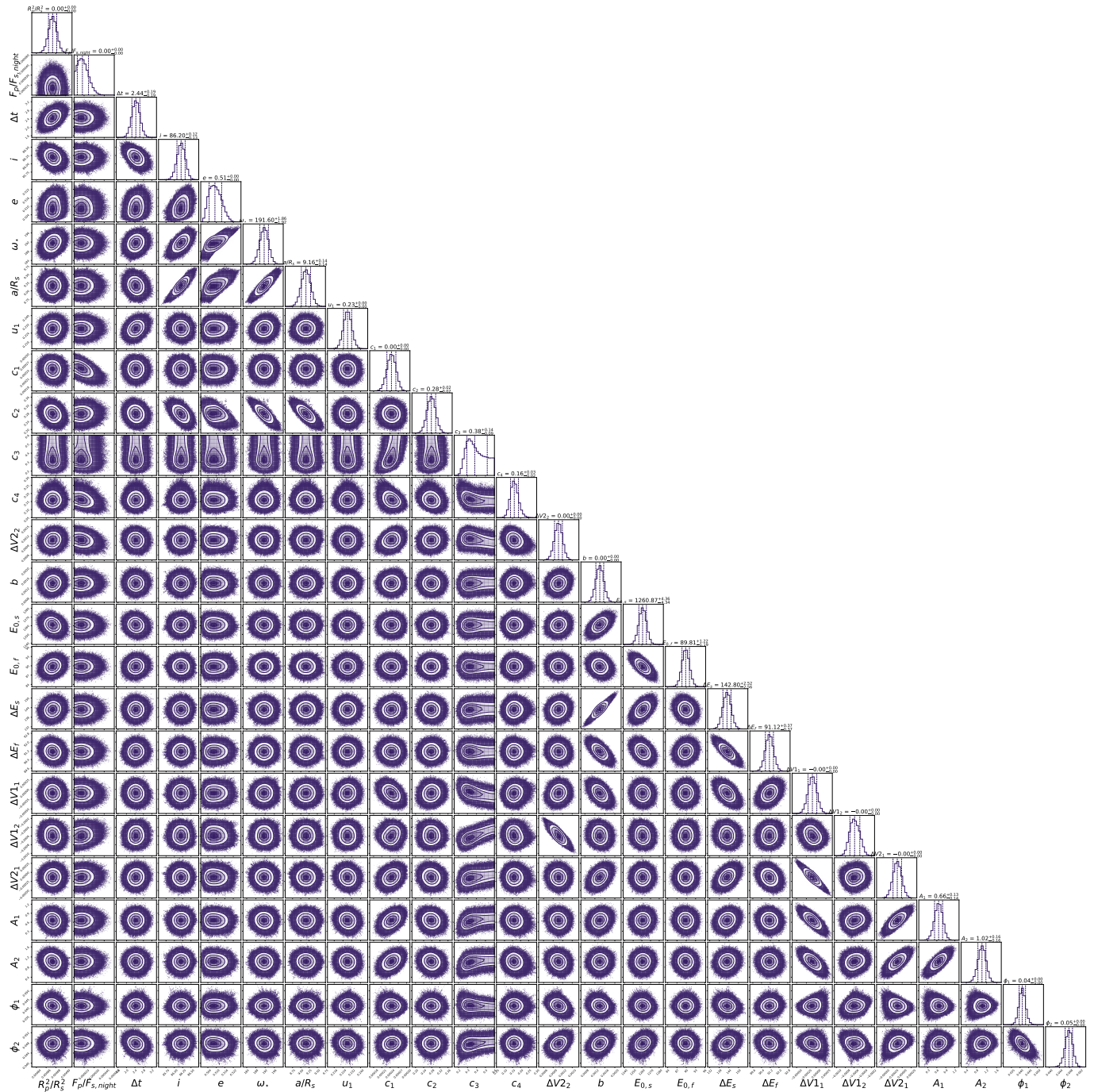


Figure 15. Corner-corner plot of the parameters retrieved from HAT-P-2b's white light-curve.

Arcangeli, J., Désert, J.-M., Parmentier, V., et al. 2019, *A&A*, 625, A136, doi: [10.1051/0004-6361/201834891](https://doi.org/10.1051/0004-6361/201834891)

Astropy Collaboration, Robitaille, T. P., Tollerud, E. J., et al. 2013, *A&A*, 558, A33, doi: [10.1051/0004-6361/201322068](https://doi.org/10.1051/0004-6361/201322068)

Bakos, G. Á., Kovács, G., Torres, G., et al. 2007, *ApJ*, 670, 826, doi: [10.1086/521866](https://doi.org/10.1086/521866)

Barat, S., Désert, J.-M., Vazan, A., et al. 2024, *Nature Astronomy*, doi: [10.1038/s41550-024-02257-0](https://doi.org/10.1038/s41550-024-02257-0)

Barker, E. A., McCullough, P., & Martel, A. R. 2009, WFC3 IR SAA Passage Behavior, WFC3 Instrument Science Report 2009-40, 26 pages

Baxter, C., Désert, J.-M., Parmentier, V., et al. 2020, *A&A*, 639, A36, doi: [10.1051/0004-6361/201937394](https://doi.org/10.1051/0004-6361/201937394)

Bell, T. J., & Cowan, N. B. 2018, *ApJL*, 857, L20, doi: [10.3847/2041-8213/aabcc8](https://doi.org/10.3847/2041-8213/aabcc8)

Beltz, H., Rauscher, E., Brogi, M., & Kempton, E. M. R. 2021, *AJ*, 161, 1, doi: [10.3847/1538-3881/abb67b](https://doi.org/10.3847/1538-3881/abb67b)

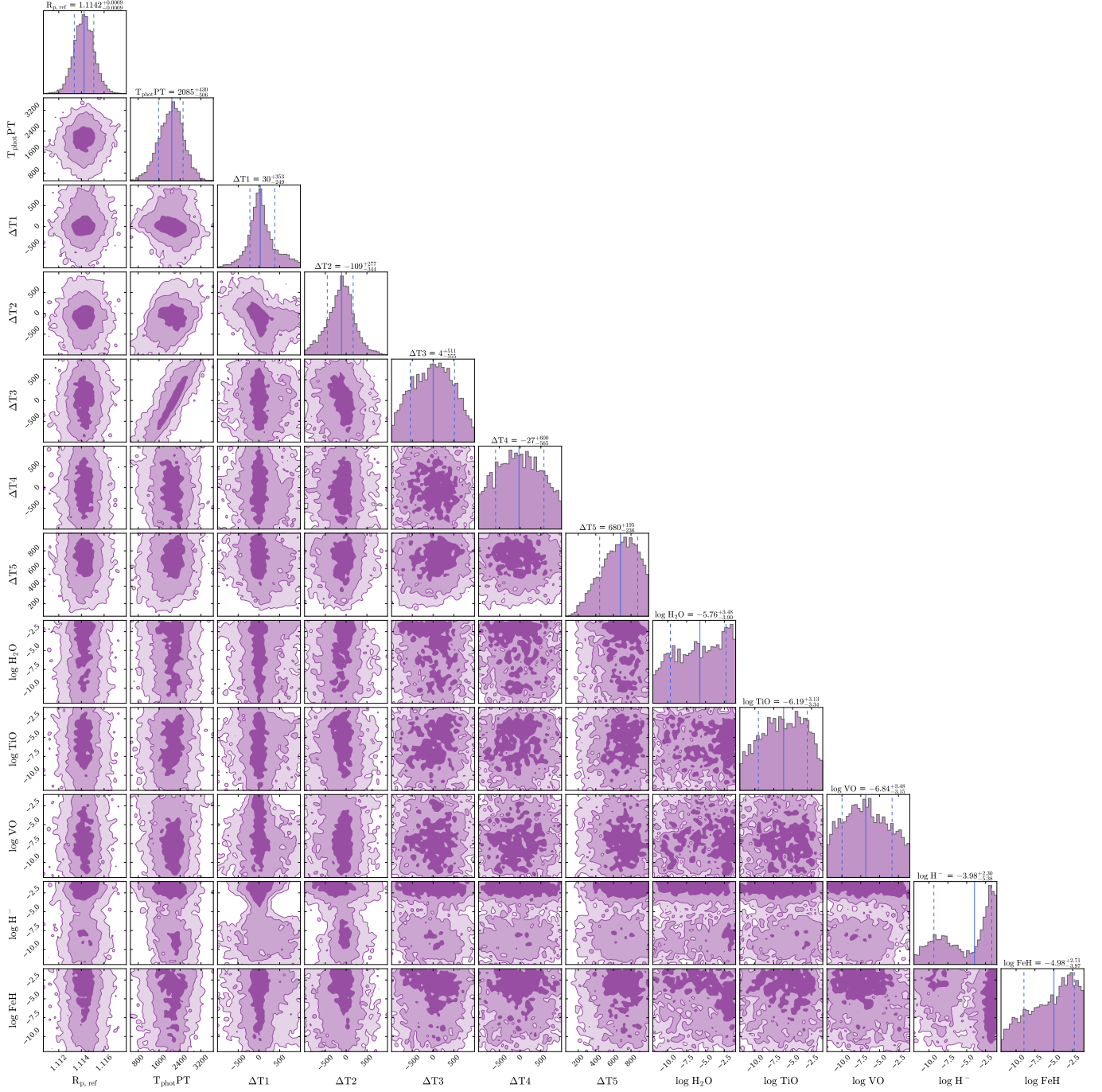


Figure 16. Corner-corner plot of the free-chemistry retrieval of the secondary eclipse spectrum. The reference radius at 0.01 bar ($R_{p,ref}$) is in Jupiter radii, ΔT_i are the temperature changes between the layers listed in Section 3.3, and the abundances of the fitted molecular species are in $\log(\text{volume mixing ratio})$.

Wavelength (μm)	F_p/F_s (ppm)	R_p^2/R_s^2	Reference
0.8	-	0.0047748 ± 0.00006	Patel & Espinoza (2022)
1.126	115^{+34}_{-33}	0.00486 ± 0.00008	This work
1.149	125 ± 22	0.00497 ± 0.00005	This work
1.181	121 ± 21	0.00486 ± 0.00005	This work
1.214	103 ± 21	0.00484 ± 0.00005	This work
1.247	129^{+21}_{-20}	0.00483 ± 0.00005	This work
1.279	177 ± 21	0.00477 ± 0.00005	This work
1.312	134 ± 21	0.00494 ± 0.00005	This work
1.344	149 ± 21	0.00492 ± 0.00005	This work
1.377	166 ± 21	0.00493 ± 0.00005	This work
1.410	143^{+22}_{-21}	0.00484 ± 0.00005	This work
1.442	154 ± 22	0.00487 ± 0.00005	This work
1.475	164^{+22}_{-23}	0.00475 ± 0.00005	This work
1.507	232 ± 23	0.00491 ± 0.00005	This work
1.540	237 ± 24	0.00485 ± 0.00006	This work
1.573	224^{+24}_{-25}	0.00494 ± 0.00006	This work
1.605	215^{+25}_{-26}	0.00488 ± 0.00006	This work
1.638	226 ± 26	0.00480 ± 0.00006	This work
3.6	996 ± 72	0.00465 ± 0.00011	Lewis et al. (2013)
4.5	971 ± 21	0.00494 ± 0.00004	de Wit et al. (2017)
5.0	710^{+290}_{-130}	-	Lewis et al. (2013)
8.0	1392 ± 95	0.00446 ± 0.00022	Lewis et al. (2013)
WFC3- averaged		0.004869 ± 0.000012	This work

Table 5. Measured eclipse depths and transit depths of HAT-P-2b at different wavelengths from this work and from the literature. We also provide the weighted wavelength-averaged transit depth of all WFC3 data. Patel & Espinoza (2022) did not measure the eclipse depth and Lewis et al. (2013) did not take any data during primary transit at $5.0 \mu\text{m}$.

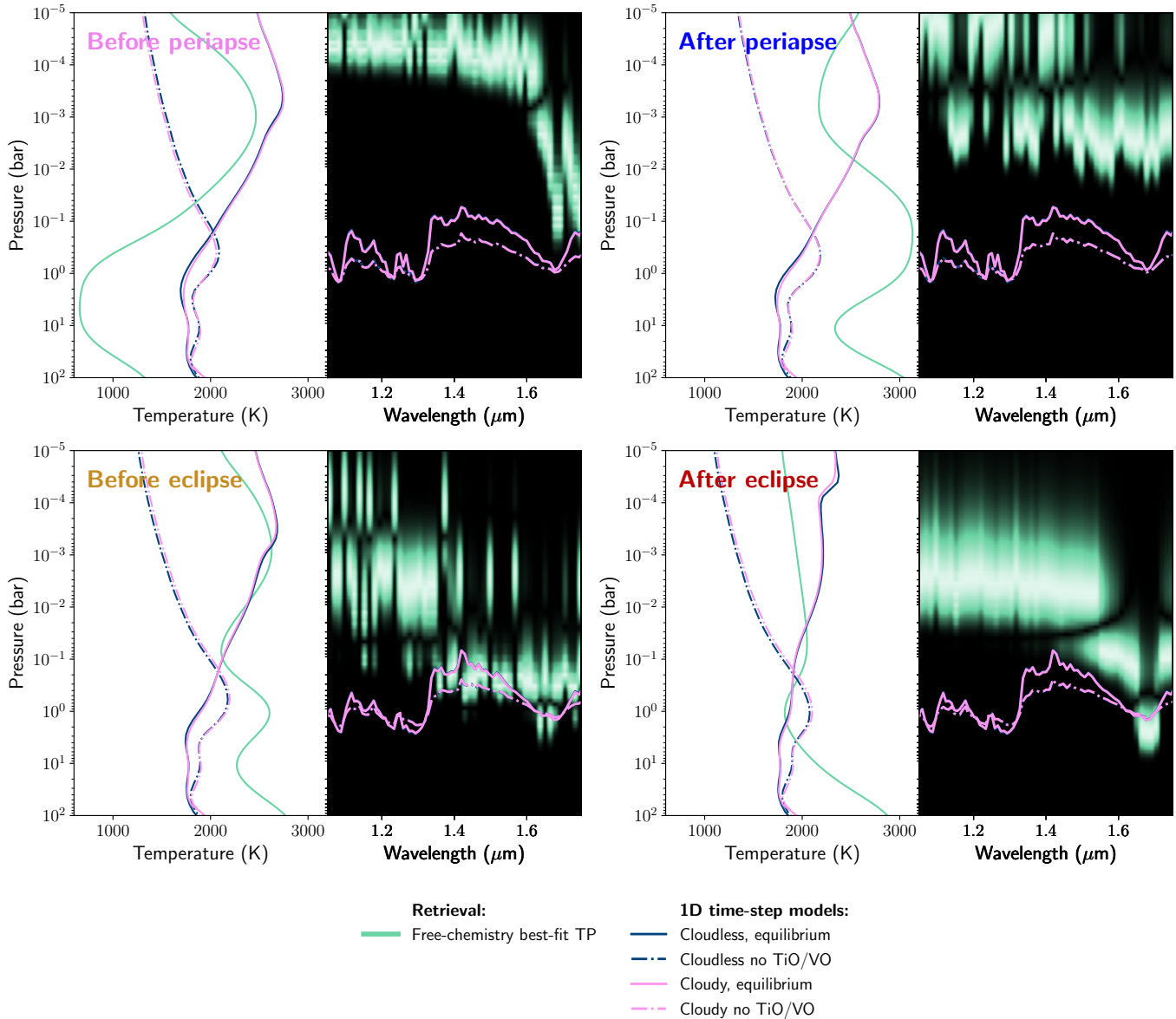


Figure 17. Best-fit temperature pressure profiles (aquamarine green) of the 1D free-chemistry retrievals of the four phase-resolved emission spectra of HAT-P-2b with the corresponding contribution functions. As a reference, the TP-profiles and the $\tau = 0.5$ contribution functions are shown for the 1D time-stepping forward models.

Beltz, H., Rauscher, E., Kempton, E. M. R., et al. 2022, *AJ*, 164, 140, doi: [10.3847/1538-3881/ac897b](https://doi.org/10.3847/1538-3881/ac897b)

Borsa, F., Fossati, L., Koskinen, T., Young, M. E., & Shulyak, D. 2021, *Nature Astronomy*, 6, 226, doi: [10.1038/s41550-021-01544-4](https://doi.org/10.1038/s41550-021-01544-4)

Bourque, M., Espinoza, N., Filippazzo, J., et al. 2021, *The Exoplanet Characterization Toolkit (ExoCTK)*, 1.0.0, Zenodo, Zenodo, doi: [10.5281/zenodo.4556063](https://doi.org/10.5281/zenodo.4556063)

Bryan, J., de Wit, J., Sun, M., de Beurs, Z. L., & Townsend, R. H. D. 2024, arXiv e-prints, arXiv:2403.08014, doi: [10.48550/arXiv.2403.08014](https://doi.org/10.48550/arXiv.2403.08014)

Buchner, J., Georgakakis, A., Nandra, K., et al. 2014, *A&A*, 564, A125, doi: [10.1051/0004-6361/201322971](https://doi.org/10.1051/0004-6361/201322971)

Caldas, A., Leconte, J., Selsis, F., et al. 2019, *A&A*, 623, A161, doi: [10.1051/0004-6361/201834384](https://doi.org/10.1051/0004-6361/201834384)

Castelli, F., & Kurucz, R. L. 2003, in *Modelling of Stellar Atmospheres*, ed. N. Piskunov, W. W. Weiss, & D. F. Gray, Vol. 210, A20, doi: [10.48550/arXiv.astro-ph/0405087](https://doi.org/10.48550/arXiv.astro-ph/0405087)

Cauley, P. W., Shkolnik, E. L., Llama, J., & Lanza, A. F. 2019, *Nature Astronomy*, 3, 1128, doi: [10.1038/s41550-019-0840-x](https://doi.org/10.1038/s41550-019-0840-x)

Challener, R. C., & Rauscher, E. 2022, *AJ*, 163, 117, doi: [10.3847/1538-3881/ac4885](https://doi.org/10.3847/1538-3881/ac4885)

- Changeat, Q., Edwards, B., Al-Refai, A. F., et al. 2022, *ApJS*, 260, 3, doi: [10.3847/1538-4365/ac5cc2](https://doi.org/10.3847/1538-4365/ac5cc2)
- Coulombe, L.-P., Benneke, B., Challener, R., et al. 2023, *Nature*, 620, 292, doi: [10.1038/s41586-023-06230-1](https://doi.org/10.1038/s41586-023-06230-1)
- Cowan, N. B., & Agol, E. 2008, *ApJL*, 678, L129, doi: [10.1086/588553](https://doi.org/10.1086/588553)
- . 2011, *ApJ*, 726, 82, doi: [10.1088/0004-637X/726/2/82](https://doi.org/10.1088/0004-637X/726/2/82)
- Cuntz, M., Saar, S. H., & Musielak, Z. E. 2000, *ApJL*, 533, L151, doi: [10.1086/312609](https://doi.org/10.1086/312609)
- de Beurs, Z. L., de Wit, J., Venner, A., et al. 2023, *AJ*, 166, 136, doi: [10.3847/1538-3881/acdf1](https://doi.org/10.3847/1538-3881/acdf1)
- de Wit, J., Lewis, N. K., Langton, J., et al. 2016, *ApJL*, 820, L33, doi: [10.3847/2041-8205/820/2/L33](https://doi.org/10.3847/2041-8205/820/2/L33)
- de Wit, J., Lewis, N. K., Knutson, H. A., et al. 2017, *ApJL*, 836, L17, doi: [10.3847/2041-8213/836/2/L17](https://doi.org/10.3847/2041-8213/836/2/L17)
- Deming, D., Wilkins, A., McCullough, P., et al. 2013, *ApJ*, 774, 95, doi: [10.1088/0004-637X/774/2/95](https://doi.org/10.1088/0004-637X/774/2/95)
- Désert, J.-M., Lecavelier des Etangs, A., Hébrard, G., et al. 2009, *ApJ*, 699, 478, doi: [10.1088/0004-637X/699/1/478](https://doi.org/10.1088/0004-637X/699/1/478)
- Désert, J.-M., Charbonneau, D., Demory, B.-O., et al. 2011, *ApJS*, 197, 14, doi: [10.1088/0067-0049/197/1/14](https://doi.org/10.1088/0067-0049/197/1/14)
- Edwards, B., Changeat, Q., Tsiaras, A., et al. 2023, *ApJS*, 269, 31, doi: [10.3847/1538-4365/ac9f1a](https://doi.org/10.3847/1538-4365/ac9f1a)
- Ehrenreich, D., Lovis, C., Allart, R., et al. 2020, *Nature*, 580, 597, doi: [10.1038/s41586-020-2107-1](https://doi.org/10.1038/s41586-020-2107-1)
- Feroz, F., Hobson, M. P., & Bridges, M. 2009, *MNRAS*, 398, 1601, doi: [10.1111/j.1365-2966.2009.14548.x](https://doi.org/10.1111/j.1365-2966.2009.14548.x)
- Figueira, P., Santerne, A., Suárez Mascareño, A., et al. 2016, *A&A*, 592, A143, doi: [10.1051/0004-6361/201628981](https://doi.org/10.1051/0004-6361/201628981)
- Foreman-Mackey, D., Hogg, D. W., Lang, D., & Goodman, J. 2013, *PASP*, 125, 306, doi: [10.1086/670067](https://doi.org/10.1086/670067)
- Fortney, J. J., Cooper, C. S., Showman, A. P., Marley, M. S., & Freedman, R. S. 2006, *ApJ*, 652, 746, doi: [10.1086/508442](https://doi.org/10.1086/508442)
- Fortney, J. J., Lodders, K., Marley, M. S., & Freedman, R. S. 2008, *ApJ*, 678, 1419, doi: [10.1086/528370](https://doi.org/10.1086/528370)
- Fortney, J. J., Marley, M. S., Lodders, K., Saumon, D., & Freedman, R. 2005, *ApJL*, 627, L69, doi: [10.1086/431952](https://doi.org/10.1086/431952)
- Fossati, L., Young, M. E., Shulyak, D., et al. 2021, *A&A*, 653, A52, doi: [10.1051/0004-6361/202140813](https://doi.org/10.1051/0004-6361/202140813)
- Fu, G., Deming, D., Lothringer, J., et al. 2021, *AJ*, 162, 108, doi: [10.3847/1538-3881/ac1200](https://doi.org/10.3847/1538-3881/ac1200)
- Fuhrmeister, B., Czesla, S., Schmitt, J. H. M. M., et al. 2023, *A&A*, 678, A1, doi: [10.1051/0004-6361/202347161](https://doi.org/10.1051/0004-6361/202347161)
- Gao, P., Marley, M. S., & Ackerman, A. S. 2018, *ApJ*, 855, 86, doi: [10.3847/1538-4357/aab0a1](https://doi.org/10.3847/1538-4357/aab0a1)
- Goodman, J., & Weare, J. 2010, *Communications in Applied Mathematics and Computational Science*, 5, 65, doi: [10.2140/camcos.2010.5.65](https://doi.org/10.2140/camcos.2010.5.65)
- Haynes, K., Mandell, A. M., Madhusudhan, N., Deming, D., & Knutson, H. 2015, *ApJ*, 806, 146, doi: [10.1088/0004-637X/806/2/146](https://doi.org/10.1088/0004-637X/806/2/146)
- Helling, C., Woters, M., Samra, D., Molaverdikhani, K., & Iro, N. 2021, *A&A*, 648, A80, doi: [10.1051/0004-6361/202039699](https://doi.org/10.1051/0004-6361/202039699)
- Hubeny, I., Burrows, A., & Sudarsky, D. 2003, *ApJ*, 594, 1011, doi: [10.1086/377080](https://doi.org/10.1086/377080)
- Huber-Feely, N., Swain, M. R., Roudier, G., & Estrela, R. 2022, *AJ*, 163, 22, doi: [10.3847/1538-3881/ac341a](https://doi.org/10.3847/1538-3881/ac341a)
- Hue, V., Gladstone, G. R., Louis, C. K., et al. 2023, *Journal of Geophysical Research (Space Physics)*, 128, e2023JA031363, doi: [10.1029/2023JA031363](https://doi.org/10.1029/2023JA031363)
- Hunter, J. D. 2007, *Computing in Science & Engineering*, 9, 90, doi: [10.1109/MCSE.2007.55](https://doi.org/10.1109/MCSE.2007.55)
- Husser, T. O., Wende-von Berg, S., Dreizler, S., et al. 2013, *A&A*, 553, A6, doi: [10.1051/0004-6361/201219058](https://doi.org/10.1051/0004-6361/201219058)
- Ilin, E., & Poppenhaeger, K. 2022, *MNRAS*, 513, 4579, doi: [10.1093/mnras/stac1232](https://doi.org/10.1093/mnras/stac1232)
- Ilin, E., Poppenhäger, K., Chebly, J., Ilić, N., & Alvarado-Gómez, J. D. 2024, *MNRAS*, 527, 3395, doi: [10.1093/mnras/stad3398](https://doi.org/10.1093/mnras/stad3398)
- Iro, N., Bézard, B., & Guillot, T. 2005, *A&A*, 436, 719, doi: [10.1051/0004-6361:20048344](https://doi.org/10.1051/0004-6361:20048344)
- Iro, N., & Deming, L. D. 2010, *ApJ*, 712, 218, doi: [10.1088/0004-637X/712/1/218](https://doi.org/10.1088/0004-637X/712/1/218)
- Ivshina, E. S., & Winn, J. N. 2022, *ApJS*, 259, 62, doi: [10.3847/1538-4365/ac545b](https://doi.org/10.3847/1538-4365/ac545b)
- Jacobs, B., Désert, J. M., Pino, L., et al. 2022, *A&A*, 668, L1, doi: [10.1051/0004-6361/202244533](https://doi.org/10.1051/0004-6361/202244533)
- Jacobs, B., Désert, J.-M., Gao, P., et al. 2023, *ApJL*, 956, L43, doi: [10.3847/2041-8213/acfee9](https://doi.org/10.3847/2041-8213/acfee9)
- John, T. L. 1988, *A&A*, 193, 189
- Karman, T., Gordon, I. E., van der Avoird, A., et al. 2019, *Icarus*, 328, 160, doi: [10.1016/j.icarus.2019.02.034](https://doi.org/10.1016/j.icarus.2019.02.034)
- Kass, R. E., & Raftery, A. E. 1995, *Journal of the American Statistical Association*, Vol. 90, No. 430. (Jun., 1995), pp. 773-795., 90, 773, doi: [10.2307/2291091](https://doi.org/10.2307/2291091)
- Kataria, T., Showman, A. P., Lewis, N. K., et al. 2013, *ApJ*, 767, 76, doi: [10.1088/0004-637X/767/1/76](https://doi.org/10.1088/0004-637X/767/1/76)
- Klein, B., Donati, J.-F., Moutou, C., et al. 2021, *MNRAS*, 502, 188, doi: [10.1093/mnras/staa3702](https://doi.org/10.1093/mnras/staa3702)
- Kreidberg, L. 2015a, *PASP*, 127, 1161, doi: [10.1086/683602](https://doi.org/10.1086/683602)
- . 2015b, *PASP*, 127, 1161, doi: [10.1086/683602](https://doi.org/10.1086/683602)
- Kreidberg, L., Bean, J. L., Désert, J.-M., et al. 2014, *Nature*, 505, 69, doi: [10.1038/nature12888](https://doi.org/10.1038/nature12888)
- Kreidberg, L., Line, M. R., Parmentier, V., et al. 2018, *AJ*, 156, 17, doi: [10.3847/1538-3881/aac3df](https://doi.org/10.3847/1538-3881/aac3df)
- Kurucz, R. L. 1993, *SYNTHE spectrum synthesis programs and line data*

- Lewis, N. K., Showman, A. P., Fortney, J. J., Knutson, H. A., & Marley, M. S. 2014, *ApJ*, 795, 150, doi: [10.1088/0004-637X/795/2/150](https://doi.org/10.1088/0004-637X/795/2/150)
- Lewis, N. K., Knutson, H. A., Showman, A. P., et al. 2013, *ApJ*, 766, 95, doi: [10.1088/0004-637X/766/2/95](https://doi.org/10.1088/0004-637X/766/2/95)
- Lewis, N. K., Wakeford, H. R., MacDonald, R. J., et al. 2020, *ApJL*, 902, L19, doi: [10.3847/2041-8213/abb77f](https://doi.org/10.3847/2041-8213/abb77f)
- Lodders, K. 2003, *ApJ*, 591, 1220, doi: [10.1086/375492](https://doi.org/10.1086/375492)
- Lodders, K., & Fegley, B. 2002, *Icarus*, 155, 393, doi: [10.1006/icar.2001.6740](https://doi.org/10.1006/icar.2001.6740)
- Lothringer, J. D., Barman, T., & Koskinen, T. 2018, *ApJ*, 866, 27, doi: [10.3847/1538-4357/aadd9e](https://doi.org/10.3847/1538-4357/aadd9e)
- MacDonald, R. J. 2023, *The Journal of Open Source Software*, 8, 4873, doi: [10.21105/joss.04873](https://doi.org/10.21105/joss.04873)
- MacDonald, R. J., & Madhusudhan, N. 2017, *MNRAS*, 469, 1979, doi: [10.1093/mnras/stx804](https://doi.org/10.1093/mnras/stx804)
- Marley, M. S., & McKay, C. P. 1999, *Icarus*, 138, 268, doi: [10.1006/icar.1998.6071](https://doi.org/10.1006/icar.1998.6071)
- Mayorga, L. C., Batalha, N. E., Lewis, N. K., & Marley, M. S. 2019, *AJ*, 158, 66, doi: [10.3847/1538-3881/ab29fa](https://doi.org/10.3847/1538-3881/ab29fa)
- Mayorga, L. C., Robinson, T. D., Marley, M. S., May, E. M., & Stevenson, K. B. 2021, *ApJ*, 915, 41, doi: [10.3847/1538-4357/abff50](https://doi.org/10.3847/1538-4357/abff50)
- McCullough, P., & MacKenty, J. 2012, *Considerations for using Spatial Scans with WFC3*, Instrument Science Report WFC3 2012-08, 17 pages
- McKemmish, L. K., Masseron, T., Hoeijmakers, H. J., et al. 2019, *MNRAS*, 488, 2836, doi: [10.1093/mnras/stz1818](https://doi.org/10.1093/mnras/stz1818)
- McKemmish, L. K., Yurchenko, S. N., & Tennyson, J. 2016, *MNRAS*, 463, 771, doi: [10.1093/mnras/stw1969](https://doi.org/10.1093/mnras/stw1969)
- Mikal-Evans, T., Sing, D. K., Barstow, J. K., et al. 2022, *Nature Astronomy*, 6, 471, doi: [10.1038/s41550-021-01592-w](https://doi.org/10.1038/s41550-021-01592-w)
- Newville, M., Stensitzki, T., Allen, D. B., & Ingarciola, A. 2014, *LMFIT: Non-Linear Least-Square Minimization and Curve-Fitting for Python*, 0.8.0, Zenodo, Zenodo, doi: [10.5281/zenodo.11813](https://doi.org/10.5281/zenodo.11813)
- Pál, A., Bakos, G. Á., Torres, G., et al. 2010, *MNRAS*, 401, 2665, doi: [10.1111/j.1365-2966.2009.15849.x](https://doi.org/10.1111/j.1365-2966.2009.15849.x)
- pandas development team, T. 2020, *pandas-dev/pandas: Pandas, latest*, Zenodo, doi: [10.5281/zenodo.3509134](https://doi.org/10.5281/zenodo.3509134)
- Parmentier, V., & Crossfield, I. J. M. 2018, in *Handbook of Exoplanets*, ed. H. J. Deeg & J. A. Belmonte, 116, doi: [10.1007/978-3-319-55333-7_116](https://doi.org/10.1007/978-3-319-55333-7_116)
- Parmentier, V., Line, M. R., Bean, J. L., et al. 2018, *A&A*, 617, A110, doi: [10.1051/0004-6361/201833059](https://doi.org/10.1051/0004-6361/201833059)
- Patel, J. A., & Espinoza, N. 2022, *AJ*, 163, 228, doi: [10.3847/1538-3881/ac5f55](https://doi.org/10.3847/1538-3881/ac5f55)
- Piette, A. A. A., & Madhusudhan, N. 2020, *MNRAS*, 497, 5136, doi: [10.1093/mnras/staa2289](https://doi.org/10.1093/mnras/staa2289)
- Pino, L., Brogi, M., Désert, J. M., et al. 2022, *A&A*, 668, A176, doi: [10.1051/0004-6361/202244593](https://doi.org/10.1051/0004-6361/202244593)
- Polyansky, O. L., Kyuberis, A. A., Zobov, N. F., et al. 2018, *MNRAS*, 480, 2597, doi: [10.1093/mnras/sty1877](https://doi.org/10.1093/mnras/sty1877)
- Robinson, T. D., & Marley, M. S. 2014, *ApJ*, 785, 158, doi: [10.1088/0004-637X/785/2/158](https://doi.org/10.1088/0004-637X/785/2/158)
- Rogers, T. M., & Komacek, T. D. 2014, *ApJ*, 794, 132, doi: [10.1088/0004-637X/794/2/132](https://doi.org/10.1088/0004-637X/794/2/132)
- Sánchez-López, A., Lin, L., Snellen, I. A. G., et al. 2022, *A&A*, 666, L1, doi: [10.1051/0004-6361/202244416](https://doi.org/10.1051/0004-6361/202244416)
- Saumon, D., & Marley, M. S. 2008, *ApJ*, 689, 1327, doi: [10.1086/592734](https://doi.org/10.1086/592734)
- Saur, J., Grambusch, T., Duling, S., Neubauer, F. M., & Simon, S. 2013, *A&A*, 552, A119, doi: [10.1051/0004-6361/201118179](https://doi.org/10.1051/0004-6361/201118179)
- Schmidt, S. J., Kowalski, A. F., Hawley, S. L., et al. 2012, *ApJ*, 745, 14, doi: [10.1088/0004-637X/745/1/14](https://doi.org/10.1088/0004-637X/745/1/14)
- Seager, S., Richardson, L. J., Hansen, B. M. S., et al. 2005, *ApJ*, 632, 1122, doi: [10.1086/444411](https://doi.org/10.1086/444411)
- Shkolnik, E., Bohlender, D. A., Walker, G. A. H., & Collier Cameron, A. 2008, *ApJ*, 676, 628, doi: [10.1086/527351](https://doi.org/10.1086/527351)
- Showman, A. P., Fortney, J. J., Lian, Y., et al. 2009, *ApJ*, 699, 564, doi: [10.1088/0004-637X/699/1/564](https://doi.org/10.1088/0004-637X/699/1/564)
- Southworth, J. 2010, *MNRAS*, 408, 1689, doi: [10.1111/j.1365-2966.2010.17231.x](https://doi.org/10.1111/j.1365-2966.2010.17231.x)
- Stevenson, K. B., & Fowler, J. 2019, *Analyzing Eight Years of Transiting Exoplanet Observations Using WFC3's Spatial Scan Monitor*, Instrument Science Report WFC3 2019-12, 16 pages. <https://arxiv.org/abs/1910.02073>
- Stevenson, K. B., Harrington, J., Nymeyer, S., et al. 2010, *Nature*, 464, 1161, doi: [10.1038/nature09013](https://doi.org/10.1038/nature09013)
- Stevenson, K. B., Désert, J.-M., Line, M. R., et al. 2014, *Science*, 346, 838, doi: [10.1126/science.1256758](https://doi.org/10.1126/science.1256758)
- STScI Development Team. 2013, *pysynphot: Synthetic photometry software package*, Astrophysics Source Code Library, record ascl:1303.023. <http://ascl.net/1303.023>
- Sulaiman, A. H., Szalay, J. R., Clark, G., et al. 2023, *Geophys. Res. Lett.*, 50, e2023GL103456, doi: [10.1029/2023GL103456](https://doi.org/10.1029/2023GL103456)
- Taylor, J., Parmentier, V., Irwin, P. G. J., et al. 2020, *MNRAS*, 493, 4342, doi: [10.1093/mnras/staa552](https://doi.org/10.1093/mnras/staa552)
- Townsend, R., & Lopez, A. 2023, *Journal of Open Source Software*, 8, 4602, doi: [10.21105/joss.04602](https://doi.org/10.21105/joss.04602)
- Tsai, S.-M., Steinrueck, M., Parmentier, V., Lewis, N., & Pierrehumbert, R. 2023, *MNRAS*, 520, 3867, doi: [10.1093/mnras/stad214](https://doi.org/10.1093/mnras/stad214)
- Tsantaki, M., Sousa, S. G., Santos, N. C., et al. 2014, *A&A*, 570, A80, doi: [10.1051/0004-6361/201424257](https://doi.org/10.1051/0004-6361/201424257)
- Tsiaras, A., Waldmann, I. P., Rocchetto, M., et al. 2016, *ApJ*, 832, 202, doi: [10.3847/0004-637X/832/2/202](https://doi.org/10.3847/0004-637X/832/2/202)

- Van Rossum, G., & Drake Jr, F. L. 1995, Python reference manual (Centrum voor Wiskunde en Informatica Amsterdam)
- Vidotto, A. A. 2020, in *Solar and Stellar Magnetic Fields: Origins and Manifestations*, ed. A. Kosovichev, S. Strassmeier, & M. Jardine, Vol. 354, 259–267, doi: [10.1017/S1743921319009979](https://doi.org/10.1017/S1743921319009979)
- Virtanen, P., Gommers, R., Oliphant, T. E., et al. 2020, *Nature Methods*, 17, 261, doi: [10.1038/s41592-019-0686-2](https://doi.org/10.1038/s41592-019-0686-2)
- Visscher, C. 2012, *ApJ*, 757, 5, doi: [10.1088/0004-637X/757/1/5](https://doi.org/10.1088/0004-637X/757/1/5)
- Wakeford, H. R., Sing, D. K., Evans, T., Deming, D., & Mandell, A. 2016, *ApJ*, 819, 10, doi: [10.3847/0004-637X/819/1/10](https://doi.org/10.3847/0004-637X/819/1/10)
- Wardenier, J. P., Parmentier, V., Lee, E. K. H., Line, M. R., & Gharib-Nezhad, E. 2021, *MNRAS*, 506, 1258, doi: [10.1093/mnras/stab1797](https://doi.org/10.1093/mnras/stab1797)
- Waskom, M. L. 2021, *Journal of Open Source Software*, 6, 3021, doi: [10.21105/joss.03021](https://doi.org/10.21105/joss.03021)
- Wende, S., Reiners, A., Seifahrt, A., & Bernath, P. F. 2010, *A&A*, 523, A58, doi: [10.1051/0004-6361/201015220](https://doi.org/10.1051/0004-6361/201015220)
- Wyttenbach, A., Mollière, P., Ehrenreich, D., et al. 2020, *A&A*, 638, A87, doi: [10.1051/0004-6361/201937316](https://doi.org/10.1051/0004-6361/201937316)
- Yadav, R. K., & Thorngren, D. P. 2017, *ApJL*, 849, L12, doi: [10.3847/2041-8213/aa93fd](https://doi.org/10.3847/2041-8213/aa93fd)
- Zhou, Y., Apai, D., Lew, B. W. P., & Schneider, G. 2017, *AJ*, 153, 243, doi: [10.3847/1538-3881/aa6481](https://doi.org/10.3847/1538-3881/aa6481)